Circuits and Systems
Mekelweg 4,
2628 CD Delft
The Netherlands
https://sps.ewi.tudelft.nl/

SPS-2024-00

M.Sc. Thesis

Towards optimizing PMCW Radar: Low Complexity Correlation and Enhanced Frame Design

Hanqing Wu

Abstract

The rapid development of Advanced Driver Assistance Systems (ADAS) necessitates enhanced performance in automotive radar systems, with Phase Modulated Continuous Wave (PMCW) radar emerging as a key technology due to its high resolution, interference resistance, and robust performance. Despite these advantages, PMCW radar faces challenges such as high computational complexity and Doppler-induced range sidelobes. This thesis addresses these challenges by proposing an adaptive block FFT correlation method to reduce computational complexity and enhance processing efficiency, ensuring reliable target detection. Additionally, we tackle Doppler-induced range sidelobes by introducing code diversity and novel frame designs for MIMO systems, leveraging cyclic shifts and Hadamard matrices to balance sidelobe attenuation and sequence set size requirements. Through extensive analysis and simulations, the proposed methods demonstrate significant improvements in radar performance, especially in detecting weak targets behind strong reflectors. The findings contribute to developing more efficient, reliable, and scalable PMCW radar systems for advanced automotive applications.

Towards optimizing PMCW Radar: Low Complexity Correlation and Enhanced Frame Design

Thesis

submitted in partial fulfillment of the
requirements for the degree of

Master of Science

in

Electrical Engineering

by

Hanqing Wu
born in Yangzhou, China

This work was performed in:

Circuits and Systems Group
Department of Microelectronics
Faculty of Electrical Engineering, Mathematics and Computer Science
Delft University of Technology

Delft University of Technology

Delft University of Technology
Department of
Microelectronics

The undersigned hereby certify that they have read and recommend to the Faculty of Electrical Engineering, Mathematics and Computer Science for acceptance a thesis entitled **"Towards optimizing PMCW Radar: Low Complexity Correlation and Enhanced Frame Design"** by **Hanqing Wu** in partial fulfillment of the requirements for the degree of **Master of Science**.

Dated: 22/08/2024

Chairman: _____
prof. dr. ir. G.J.T.Leus

Advisor: _____
dr. ir. A.Pandharipande

Committee Members: _____
dr. ir. F. Fioranelli

_____

Abstract

The rapid development of Advanced Driver Assistance Systems (ADAS) necessitates enhanced performance in automotive radar systems, with Phase Modulated Continuous Wave (PMCW) radar emerging as a key technology due to its high resolution, interference resistance, and robust performance. Despite these advantages, PMCW radar faces challenges such as high computational complexity and Doppler-induced range sidelobes. This thesis addresses these challenges by proposing an adaptive block FFT correlation method to reduce computational complexity and enhance processing efficiency, ensuring reliable target detection. Additionally, we tackle Doppler-induced range sidelobes by introducing code diversity and novel frame designs for MIMO systems, leveraging cyclic shifts and Hadamard matrices to balance sidelobe attenuation and sequence set size requirements. Through extensive analysis and simulations, the proposed methods demonstrate significant improvements in radar performance, especially in detecting weak targets behind strong reflectors. The findings contribute to developing more efficient, reliable, and scalable PMCW radar systems for advanced automotive applications.

Acknowledgments

Time flies, and my time at TU Delft has now come to an end. These two years have been a journey of exploration, where I delved into various areas of signal processing, including acoustic, biomedical, and radar signals. Though challenging, it was equally rewarding. I am grateful to many people who made this journey possible.

First of all, I wish to express my deepest appreciation to my supervisors, Geert Leus and Ashish Pandharipande, for their invaluable guidance and support. Geert is an exceptional teacher, and I still remember the awe I felt when he derived formulas on the blackboard during SDSP class. I am incredibly grateful for all the courses I took with Geert, and for his patience in helping me refine my thesis, addressing my concerns, and offering in-depth and high-level feedback. Ashish gave me considerable freedom to explore the PMCW field and encouraged me to pursue directions that intrigued me. Throughout the thesis process, Ashish provided invaluable assistance, offering a wealth of learning resources and suggestions that inspired and guided me. His unique perspectives and profound insights continually sparked fresh ideas, driving me toward refinement and advancement in my research. Additionally, I extend my gratitude to Francesco Fioranelli for joining my thesis committee. It feels like a full circle as my first course at TU Delft, "System Engineering," was under his guidance, bringing a meaningful sense of closure to my academic journey.

My academic journey was not undertaken alone. I am deeply grateful to Jeroen and Shengzhi for their papers, which were instrumental in providing me with a solid foundation in the PMCW field. Their work served as crucial reference points, enabling me to grasp the complex concepts and methodologies necessary to navigate and contribute meaningfully to this area of research. I also want to thank Pavan and Jiaqi, who studied and discussed ideas with me daily in the NXP intern area, as we encouraged each other along the way. A special thanks to Çağan for our discussions and for working with me on simulations. I walked alongside many esteemed companions during these two years, and I am thankful to all the classmates and friends I collaborated with. The days spent gathering and chatting with everyone brought me great happiness.

Lastly, I extend my profound gratitude to my parents for their unwavering moral support. Due to the time difference, we could only video chat on weekends, but their love and encouragement were never limited by the screen. Furthermore, I am deeply thankful to Shengzhe for his years of companionship and encouragement as we journeyed together from Yangzhou to Harbin and now to Europe. His presence during my defense, traveling all the way from Switzerland, made me feel as if I had family by my side.

As my journey at TU Delft nears its closure, it marks the beginning of a new chapter in my life. As I wrote at my undergraduate graduation, I hope we continue to engage with the world with enthusiasm and always walk on paths adorned with flowers.

Hanqing Wu
Delft, The Netherlands
22/08/2024

Contents

List of Figures

List of Tables

1 Introduction

Advanced Driver Assistance Systems (ADAS) are technologies that assist drivers with safe operations of a vehicle. Over the past decade, ADAS have gained significant interest from the automotive industry due to their potential to enable safe, automated, and autonomous driving, ultimately making transportation safer for all road users [2].

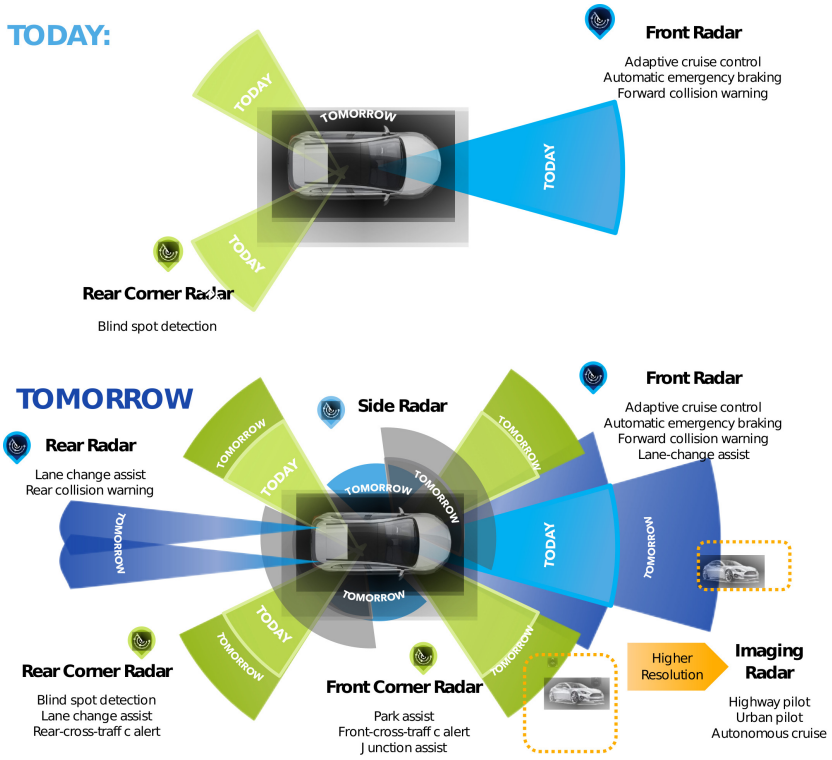

Figure 1.1: ADAS system (Source: NXP Semiconductors)

Based on the functionality of the driving automation system, ADAS can be classified into levels ranging from 0 to 5 as defined by the SAE standard [3]. Level 0 ADAS do not perform any vehicle control tasks but provide information to the driver, helping monitor the surrounding environment or the driver's status. Levels 1 and 2, known as "driver support" features, assist with specific driving functions such as Adaptive Cruise Control, Emergency Brake Assist, Lane Keeping, Autonomous Obstacle Avoidance, Highway Assist, and Autonomous Parking [4]. While these levels still require driver authority, they enhance safety and convenience. Levels 3 to 5 are considered "automated driving" features. At these levels, ADAS perform the entire dynamic driving task on a sustained basis while engaged. Level 5 represents full automation, where the vehicle requires no driver intervention, featuring comprehensive sensing coverage,

and advanced decision-making intelligence. In this stage, vehicles can operate without any driver controls, transforming the driver into a passenger who simply sets a destination and relaxes while the vehicle transports them [4].

The automotive industry, including car manufacturers and tier-1 and tier-2 suppliers (such as radar module and radar chip suppliers), is heavily invested in advancing ADAS towards highly automated driving systems, with the ultimate goal of achieving fully autonomous, self-driving cars. One example of this ADAS development is shown in Figure 1.1.

1.1 Requirements for Automotive Radar Systems

As automated driving technology advances, automotive radar systems are becoming increasingly sophisticated, serving as essential environment sensors. These systems enable vehicles to accurately perceive their surroundings by detecting objects, measuring distance, velocity, and angle, and mitigating interference. Modern automotive radar not only enhances driver-assistance features but also paves the way for fully autonomous driving. This section highlights the key advancements and capabilities shaping the future of automotive radar technology.

- **High-Resolution Capabilities**: Automotive radar systems must achieve precise measurements of radial distance, velocity, and angle to support ADAS effectively [5]. High Doppler resolution is essential for distinguishing different radial velocities, enabling the radar to differentiate between objects moving at varying speeds. This capability is crucial for applications like adaptive cruise control, which ensures safe and efficient driving by maintaining appropriate distances between vehicles. Additionally, higher angular resolution, facilitated by multiple input multiple output (MIMO) configurations, is vital for resolving closely spaced targets [6]. By achieving finer angular resolution, radar sensors can discern multiple scattering centers on objects, such as vehicles, which is crucial for tasks like precise lane keeping and collision avoidance.

- **High Dynamic Range**: Detection and classification of vulnerable road users such as pedestrians and cyclists, particularly in urban environments, require radar sensors to be sensitive to weak targets. This necessitates a higher dynamic range to detect reflected signals that are significantly lower in power compared to those from vehicles [7].

- **Robustness to Interference**: Mutual Interference (MI) occurs when radar transmissions from one vehicle interfere with those of another, potentially masking target signals and reducing radar performance [8]. As radar sensors proliferate in vehicles, effective MI mitigation is crucial for reliable operation at higher levels of automation.

- **Low-Cost Hardware**: To enable widespread adoption across vehicle fleets and achieve comprehensive 360° coverage, radar sensors must be cost-effective to manufacture. This requires simplified signal generation, minimal Analog-to-Digital

Converters (ADCs), and lower-megahertz range sampling frequencies to reduce hardware costs while maintaining performance [5].

1.2 Transition to Digitally Modulated Radar Systems

Driven by the improved requirements of ADAS, the transition from analog radar, specifically Frequency Modulated Continuous Wave (FMCW) radar, to Digitally Modulated Radar (DMR) systems in automotive applications has become imperative [9].

1.2.1 Limitations of Analog Radar

FMCW radar has been the predominant technology in automotive applications due to its maturity, ease of implementation, and low power consumption [9]. However, the advancements in ADAS have significantly increased the performance demands for radar systems, which are challenging for traditional analog radar systems to achieve.

One of the primary limitations of FMCW radar is its susceptibility to radar-to-radar interference, which becomes more problematic as the number of radar-equipped vehicles increases [8]. Additionally, achieving high resolution and longer detection ranges with FMCW requires reducing chirp durations, which complicates system design and degrades performance [10]. The growing number of transmit antennas in MIMO configurations further exacerbates the challenge by decreasing the maximum unambiguous radial velocity when traditional time multiplexing is used [10].

1.2.2 Advantages of Digitally Modulated Radar

To address these challenges, attention has increasingly turned towards digitally modulated radar systems, such as Orthogonal Frequency Division Multiplexing (OFDM) and Phase Modulated Continuous Wave (PMCW) radar. These digital modulation schemes offer several significant advantages:

- **Enhanced Interference Mitigation**: Digital modulation schemes provide better resilience to interference through techniques such as code orthogonality and advanced signal processing algorithms [8, 11]. This capability is essential in crowded environments where multiple radars may interfere with each other.
- **Higher Resolution and Range**: Digital radar systems can utilize wideband signals to achieve higher resolution and longer detection ranges without being limited by the chirp duration constraints of analog systems [11]. This allows for more precise target detection and discrimination.
- **Integration with Advanced Features**: Digitally modulated radars can seamlessly integrate with other advanced automotive features such as communication systems and sensor fusion, enhancing the overall functionality of ADAS. Additionally, one notable advantage of these radars is their ability to exploit joint communication and radar sensing (JCRS). This capability not only aids in mitigating mutual interference and facilitating ghost target removal but also improves

overall system coordination and data sharing, contributing to a more robust and reliable automotive sensing environment [12].

- **Improved Signal Processing**: Digital modulation allows most of the signal processing to be done digitally, enabling the use of advanced algorithms that enhance the radar's performance and robustness [13, 5].

1.2.3 Emergence of Digitally Modulated Radar Systems

Recent advancements in CMOS technology, low-power high-speed ADCs [14], and advanced signal processing have made it feasible to design cost-effective DMR systems that meet the increasing performance demands of the automotive industry. These technological improvements have addressed the primary impediments to the widespread adoption of digital radar in automotive applications, making it a viable and superior alternative to traditional FMCW radar.

In summary, while FMCW radar remains prevalent due to its established technology and ease of implementation, the increasing performance demands of ADAS have highlighted its limitations. Digitally modulated radar systems, with their superior interference mitigation, higher resolution and range, and greater flexibility and scalability, are becoming essential to meet these new challenges. As automotive radar technology evolves, digitally modulated radar systems will play a crucial role in advancing the capabilities of ADAS and autonomous driving, ensuring safer and more efficient driving experiences.

1.3 PMCW Radar

In this work, we focus on binary PMCW radar, which uses sequences of binary symbols mapped to 0 and 180-degree phase shifts of a continuous Radio Frequency (RF) carrier. This modulated waveform offers several advantages in both radar performance and implementation simplicity [15]. Recent designS [16, 17] in 28nm CMOS technology show that 79 GHz single-chip 2×2 MIMO PMCW radars have now become feasible. In this section, we will provide a block diagram to illustrate the PMCW MIMO radar's principles, explore its advantages, and discuss the challenges it faces.

1.3.1 PMCW Principle

The architectual overview of the MIMO PMCW system with N_{tx} transmit antennas and N_{rx} receive antennas is given in Figure 1.2. The key components are discussed below.

- **Pseudorandom Code Generator**:

In the context of radar systems, the principle of code division plays a critical role, and we focus exclusively on binary sequences, which are generated using a Pseudorandom Code Generator. It produces a set of $|S|$ binary sequences, each of length L_c, that exhibits favorable characteristics for radar applications. The binary sequence of length

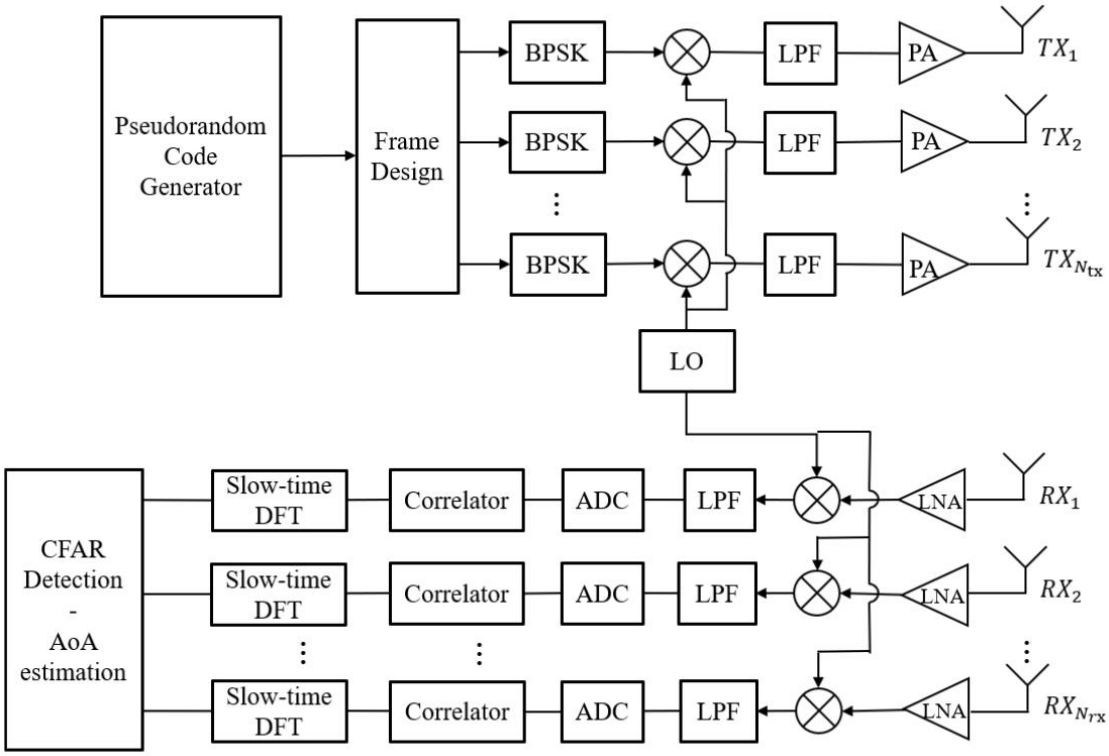

Figure 1.2: Schematic overview of the PMCW radar system

L_c is denoted as $b_0, b_1, \ldots, b_{L_c-1}$, where each symbol b_n belongs to the set { -1,+1} for $n = 0, 1, \cdots, L_c - 1$.

The performance of a radar system is significantly influenced by the properties of these sequences, particularly in terms of their auto-correlation and cross-correlation characteristics. From a radar signal processing perspective, achieving near-perfect auto-correlation and ideal cross-correlation properties is paramount. Perfect auto-correlation is characterized by a correlation function that attains its maximum value when the sequence is not shifted (i.e., at a zero shift) and yields zero for all nonzero shifts. Ideal cross-correlation requires that all sequences within the set $|S|$ be orthogonal to one another. Orthogonality implies that the cross-correlation values between any pair of distinct sequences are zero for all possible shifts. These properties are essential for maximizing peak correlation values and minimizing the range sidelobe level, which in turn enhance the accuracy and resolution of the radar system. Thus, the careful design and selection of binary sequences with these characteristics are essential for advancing radar technology and its applications.

- **Frame Design**:

Each transmitter operates by repeating the code sequence N_{acc} times to achieve coherent accumulation, thereby enhancing signal-to-Noise Ratio (SNR). This process results in what is referred to as one sample, comprising $N_{acc}L_c$ binary symbols. Subsequently, the radar system's frame is designed to produce M slow-time samples, which

are essential for Doppler processing. In state-of-the-art MIMO PMCW systems with N_{tx} transmit antennas, the samples are repeated M times across each transmitter. This repetition means that each transmitter continuously transmits the same sequence. M slow-time samples allow capturing temporal variations due to the relative motion of targets, which is essential for Doppler analysis. While repetition is a common frame design, other designs exist and will be discussed in Chapter Chapter 3. For the generalization, $b_n^{(i,m)}$ denotes the nth bit of the sequence related to the ith transmitter and mth sample.

- **BPSK Modulation**:

These discrete binary sequences are modulated onto an analog electromagnetic (EM) signal using Binary Phase-Shift Keying (BPSK) modulation. BPSK conveys data by changing the phase of a reference signal, at time instants which are multiples of T_c, where T_c is inversely proportional to the bandwidth of the transmitted signal, $T_c = \frac{1}{B}$.

$$\phi_{+1} = 0 \quad \exp(j \cdot 0) = +1 \tag{1.1}$$

$$\phi_{-1} = \pi \quad \exp(j \cdot \pi) = -1 \tag{1.2}$$

Thus, each pulse has a duration $T_r = L_c T_c$. Then we could write the transmitted baseband signal from the ith transmitter as

$$\begin{aligned} s_{i,IF}(t) &= \sum_{m=0}^{M-1} \sum_{n_{acc}=0}^{N_{acc}-1} \sum_{n=0}^{L_c-1} \exp(j\phi_{b_n^{(i,m)}}) \operatorname{rect}\left(\frac{t - nT_c - n_{acc}T_r - mT_r}{T_c}\right) \\ &= \sum_{m=0}^{M-1} \sum_{n_{acc}=0}^{N_{acc}-1} \sum_{n=0}^{L_c-1} c_n^{(i,m)} \operatorname{rect}\left(\frac{t - nT_c - n_{acc}T_r - mT_r}{T_c}\right) \quad t \in [0, T_{frame}) \end{aligned} \tag{1.3}$$

where $\phi_{b_n^{(i,m)}}$ denotes the phase corresponding to the element $b_n^{(i,m)}$ and it could be written as $c_n^{(i,m)}$. The phase is kept constant for the chip duration T_c. When the concurrent chip value changes from -1 to +1, or vice versa, a phase discontinuity occurs due to the 180-degree phase shift. Besides, T_{frame} denotes the total duration a transmission consists of M ensuing pulses, and it is given as $T_{frame} = M \cdot T_{acc} = M \cdot N_{acc} L_c T_c$.

- **Received Baseband Signals**:

The transmitted baseband signal is firstly up-converted by the Local Oscillator (LO) with the center frequency of f_c, after that it undergoes Low Pass Filter (LPF), Power Amplifier (PA). Then it transmitted as EM waves by the antennas and reflected back by the targets. The received RF signal is an amplitude-scaled and time-delayed version of the transmitted one. It is amplified by a Low-Noise Amplifier (LNA), and after that, the RF signal is down-converted by the same LO.

In the assumption, there are Q targets in total, and the qth target is represented as (R_q, v_q, θ_q), denoting the initial range, radial velocity, and angle of the qth target, respectively. The time delay caused by the qth target is given as

$$\tau_q(t) = \frac{2(R_q + v_q t)}{c} = \tau_q + \frac{2v_q}{c} t \tag{1.4}$$

where $\tau_q = \frac{2R_q}{c}$ denotes the initial round trip delay of the qth target and c represents the speed of light.

The received baseband signal of jth receiver from Q targets is

$$y_j(t) = \sum_{q=1}^{Q} \beta_q \phi_{R,\theta_q}^{j-1} \sum_{i=1}^{N_{tx}} \phi_{T,\theta_q}^{i-1} s_{i,IF}(t - \tau_q(t)) e^{-j2\pi f_c \tau_q(t)} \tag{1.5}$$

where β_q denotes the complex amplitude of the qth target, and $\phi_{T,\theta_q} = e^{j2\pi d_T \sin(\theta_q)/\lambda}$ and $\phi_{R,\theta_q} = e^{j2\pi d_R \sin(\theta_q)/\lambda}$ denotes the transmit and receive steering phase shift respectively, with d_T and d_R being the inter-element distance between the transmit antennas and the the receive antennas. For simplicity, a half-wavelength spaced Uniform Linear Array (ULA) has been selected for both the transmitter and receiver array, which means that d_T and d_R is equal to $\lambda/2$.

Then, we substitute Eq.(1.4) into Eq.(1.5), and obtain:

$$\begin{aligned} y_j(t) &= \sum_{q=1}^{Q} \beta_q \phi_{R,\theta_q}^{j-1} \sum_{i=1}^{N_{tx}} \phi_{T,\theta_q}^{i-1} s_{i,IF}(t - \tau_q - \frac{2v_q}{c}t) e^{-j2\pi f_c \tau_q} e^{-j2\pi f_c \frac{2v_q}{c} t} \\ &\approx \sum_{q=1}^{Q} \beta_q e^{-j2\pi f_c \tau_q} \phi_{R,\theta_q}^{j-1} \sum_{i=1}^{N_{tx}} \phi_{T,\theta_q}^{i-1} s_{i,IF}(t - \tau_q) e^{-j2\pi f_c \frac{2v_q}{c} t} \\ &= \sum_{q=1}^{Q} \tilde{\beta}_q \phi_{R,\theta_q}^{j-1} \sum_{i=1}^{N_{tx}} \phi_{T,\theta_q}^{i-1} s_{i,IF}(t - \tau_q) e^{j2\pi f_{d,q} t} \end{aligned} \tag{1.6}$$

Assuming $v_q \ll c$, the term $\frac{2v_q}{c}$ in $s_{i,IF}(t - \tau_q - \frac{2v_q}{c}t)$ could be omitted. The phase shift $e^{-j2\pi f_c \tau_q}$ associated to τ_q is a constant term that could be absorbed into β_q, resulting in $\tilde{\beta}_q$. The Doppler frequency shift for the qth target is denoted as $f_{d,q} = -f_c \frac{2v_q}{c} = -\frac{2v_q}{\lambda}$, where λ is the wavelength of the carrier signal. Note that a positive v_q indicates that the target is moving away, causing a frequency decrease, while a negative v_q indicates the target moving towards, causing a frequency increase.

Then the received baseband signal $\mathbf{y}(t)$ from N_{rx} receivers given as

$$\mathbf{y}(t) = \sum_{q=1}^{Q} \tilde{\beta}_q \mathbf{a}_R(\theta_q) \mathbf{a}_T(\theta_q)^T \mathbf{s}_T(t - \tau_q) \tag{1.7}$$

where transmit steering vector $\mathbf{a}_T(\theta)$, receive steering vector $\mathbf{a}_R(\theta)$, and the delayed transmitted signal $\mathbf{s}_T(t - \tau_q)$ are respectively given by:

$$\mathbf{a}_T(\theta) = \begin{bmatrix} 1 \\ \phi_{T,\theta} \\ \phi_{T,\theta}^2 \\ \vdots \\ \phi_{T,\theta}^{N_{tx}-1} \end{bmatrix}, \quad \mathbf{a}_R(\theta) = \begin{bmatrix} 1 \\ \phi_{R,\theta} \\ \phi_{R,\theta}^2 \\ \vdots \\ \phi_{R,\theta}^{N_{rx}-1} \end{bmatrix}, \quad \mathbf{s}_T(t - \tau_q) = \begin{bmatrix} s_{1,IF}(t - \tau_q) e^{j2\pi f_{d,q} t} \\ s_{2,IF}(t - \tau_q) e^{j2\pi f_{d,q} t} \\ s_{3,IF}(t - \tau_q) e^{j2\pi f_{d,q} t} \\ \vdots \\ s_{N_{tx},IF}(t - \tau_q) e^{j2\pi f_{d,q} t} \end{bmatrix}$$

- **Post-Processing for Estimating Range, Velocity, and Angle**:

The received baseband signal is firstly digitized using an Analog-to-Digital Converter (ADC), where the sampling frequency is set equal to the bit rate. This means the time interval between two consecutive samples, T_c, matches the duration of one bit. Range estimation is then conducted by correlating the sampled received signal with delayed replicas of the transmitted pseudorandom code sequence. The correlation results are coherently accumulated over N_{acc} integration periods. The peak value obtained from this accumulated correlation indicates the time delay, which is directly proportional to the distance to the target. The expressions for the maximum unambiguous range R_u, and the range resolution ΔR are as follows:

$$R_u = \frac{cT_r}{2} = \frac{cT_cL_c}{2} \tag{1.8}$$

$$\Delta R = \frac{c}{2B} = \frac{cT_c}{2} \tag{1.9}$$

The Doppler processor coherently processes consecutive correlated periods to estimate velocities of possible targets. By performing a Fast Fourier Transform (FFT) on the phase differences of M accumulated complex values, the Doppler frequency shifts between successive pulses can be extracted, allowing for accurate velocity measurements. The observation time T_{frame} determines the minimum Doppler shift observable, the maximum unambiguous velocity v_u and the Doppler resolution Δv are given by:

$$|v_u| = \frac{\lambda}{4T_r} \tag{1.10}$$

$$\Delta v = \frac{\lambda}{2T_{frame}} \tag{1.11}$$

Angular estimation, on the other hand, leverages the multiple input and output channels of the MIMO system. Beamforming techniques are applied to the received signals, forming spatial filters that enhance signals arriving from specific directions. The angular position of the target is determined by finding the direction that maximizes the received signal power.

1.3.2 PMCW Benefits

PMCW radars offer several distinct advantages in radar performance and implementation, making it a promising technology for next-generation automotive radar systems.

- **Radar Performance Advantages**: PMCW radar intrinsically avoids range-Doppler coupling, features a thumbtack-like ambiguity function, which allows for more accurate measurement of both range and velocity without mutual distortion. Additionally, PMCW radar allows MIMO implementaion in the code domain, enhancing the radar's ability to distinguish between closely spaced targets. With careful code selection, PMCW radar is inherently robust against interference due to code orthogonality, reducing the likelihood of mutual interference.

- **Implementation Simplicity**: Unlike FMCW radars, PMCW radars do not require high-speed, fast-settling frequency synthesizers or high linearity, simplifying the hardware design and potentially increasing reliability. Additionally, PMCW radar can exploit Joint Communication and Radar Sensing (JCRS) [9], facilitating the integration of communication and sensing functions. This integration helps mitigate mutual interference and remove ghost targets, thereby enhancing overall system performance.

The primary limitation for implementing PMCW radar is integrating higher sampling frequency ADCs into radar chip, which has been overcame by the advances in ADC technology [14, 16, 17]. The combination of these performance and implementation advantages makes PMCW radar a compelling choice for next-generation automotive radar systems.

1.3.3 PMCW Challenges

Despite the benefits of PMCW radar systems, optimizing performance encounters challenges such as low-latency processing, designing sequences with optimal correlation properties, mitigating Doppler effects, and reducing spillover. These difficulties influence the radar system's efficiency, accuracy, and reliability. This section explores these challenges in detail.

- **Low-Latency Receiver Processing**

An ongoing challenge in PMCW radar systems is optimizing receiver processing to handle gigasamples of data with minimal detection latency. Traditional approaches often introduce significant delays and require extensive computational resources, complicating real-time data management. To meet the demands of modern applications like autonomous driving and real-time surveillance, it's crucial to develop new processing techniques that can efficiently manage high data throughput while minimizing latency. These methods must also be computationally efficient and maintain a low memory footprint, ensuring that radar systems remain both scalable and high-performing without excessive complexity.

- **Designing Good Code Sequences**

For probing binary sequence sets, it is essential to achieve good periodic auto- and cross-correlation properties to accurately extract range information and separate signals from different antennas at the receiver. Selecting appropriate code sequences is critical for achieving high dynamic range in range estimation, with the goal of generating codes that exhibit impulse-like autocorrelation and zero cross-correlation [18, 19]. However, no perfect binary sequence possesses both properties simultaneously, as limited by the Welch bound [20]. Additionally, large sequence set sizes and available code lengths are important considerations as well.

Unfortunately, many well-known periodic binary sequences, such as Almost Perfect Autocorrelation Sequences (APAS) [21], possess good autocorrelation properties but lack desirable cross-correlation characteristics. Constructive periodic binary sequence

sets like Gold sequences offer good auto- and cross-correlation properties, but their lengths are restrictively fixed at $2^n - 1$ [22]. Zero-Correlation Zone (ZCZ) sequences are designed to provide ideal correlation responses within a specific zone, but this high-performance zone is limited in comparison to the overall code length L_c [23].

In contrast, computational algorithms can be employed to design periodic binary sequence sets with arbitrary period lengths. The integrated sidelobe level (ISL) is a commonly used criterion for designing probing sequence sets for MIMO PMCW radar systems [24]. However, minimizing the ISL criterion under the binary constraint is an NP-hard and high-dimensional optimization problem. Many existing computational algorithms are unsuitable for designing long binary sequence sets due to their high computational complexities. Even in [25], where the FFT is used to implement the proposed algorithm and enhance computational efficiency, the computational complexity remains high.

To conclude, it is still challenging to design binary sequence sets that simultaneously achieve good auto- and cross-correlation properties, accommodate large set sizes, and are computationally feasible for long lengths. Existing sequences and algorithms either fall short in correlation characteristics or are limited by fixed lengths and high computational demands. Overcoming these challenges is crucial for advancing the performance and applicability of PMCW radar systems.

- **Mitigating Doppler Effects**

When a target is moving relative to the radar, Doppler information is typically derived from Fourier analysis of the slow-time domain. However, the Doppler phase shift remains in the fast-time domain after mixing with the carrier wave. This additive phase shift on the binary codes significantly reduces the orthogonality between different code sets and the self-matching of the code itself [26]. The primary consequences of the Doppler effect, due to imperfections in autocorrelation and non-orthogonality, are a decrease in target peak power and an increase in range sidelobes [27]. Consequently, the Doppler phase shift results in a decreased peak-to-sidelobe ratio, which is undesirable to detect both large, highly reflective targets (e.g., trucks) and smaller targets (e.g., pedestrians) simultaneously. Thus, mitigating the Doppler effect is crucial for enhancing radar performance in these applications.

To attenuate the range sidelobes caused by the Doppler phase shift, a solution has been proposed in [26]. This method compensates for the Doppler frequency shift remaining in the fast-time domain by first applying an FFT to the slow-time domain. Subsequently, the phases of the chip series are adjusted for each Doppler frequency cell by multiplying them with a formulated compensation term. Although this approach achieves significant attenuation of range sidelobes, it also increases the computational load, as it requires compensating the Doppler phase shift on all samples before range processing.

Another low-complexity solution that requires no modifications to the radar's analog front-end and no additional digital processing has been proposed in [18]. This method attenuates sidelobes by varying the transmitted code sequence for each slow-time repetition. However, implementing this solution for PMCW radar is challenging because it requires a sufficiently large family of code sequences of the same length with excellent

periodic auto-correlation and cross-correlation properties. This requirement becomes even more demanding when applied to large MIMO systems.

Thus, mitigating the Doppler shift effect is still challenging since current existing solutions could not achieve a good balance between attenuating the sidelobe level and retaining computational efficiency. It is necessary to seek other effective solutions to mitigate the Doppler effect, especially those suitable for large MIMO systems.

- **Mitigating Spillover**

Since PMCW is a continuous wave radar solution, the transmitter (TX) and receiver (RX) operate simultaneously, resulting in leakage from the transmitted signal to the receiver [28, 29]. This leakage, known as spillover, is several orders of magnitude higher than the expected radar reflections and can cause ghost targets, missed detections, and saturation of the ADC [17]. Therefore, it is crucial to mitigate self-interference.

The paper [30] discusses an analog spatial nulling method to mitigate self-interference in radar systems by projecting the received signal onto the null space of the interference channel. While this reduces near-field spillover, it inadvertently filters far-field signals, impacting radar sensing where it primarily occurs. Further, [29] describes a technique that uses an analog feedback loop and a vector modulator for phase adjustment to attenuate transmitter leakage by 27.5 dB. The method involves adjusting the delay and phase of a TX signal copy to cancel the spillover at the receiver. The main drawback is that nonidealities in amplitude and phase adjustments, especially at mm-wave frequencies, can significantly affect the cancellation loop's performance. Finally, [31] outlines a mixed-signal approach to reduce transmitter leakage in PMCW MIMO radars by using digital spillover estimation and generating cancellation signals delivered via a DAC post-mixer. This method improves sensitivity and simplifies the ADC resolution requirements. However, the complexity of digital computations and the precision of the DAC's resolution may impact its overall efficacy.

In conclusion, current existing techniques present advantages and trade-offs that must be carefully considered to enhance radar performance. However, effective solutions must balance spillover attenuation with computational efficiency and adaptability to system constraints. Thus, mitigating self-interference in PMCW radar systems is still a significant challenge.

1.4 Contributions

PMCW radar systems, while offering numerous benefits, encounter significant challenges in range processing and Doppler effect mitigation. The high complexity of modern correlators, often involving FFTs with a complexity of $\mathcal{O}(L_c \log L_c)$, poses difficulties, particularly with large sequence lengths required for high range and fine velocity resolution. Furthermore, Doppler phase shifts in the fast-time domain reduce the orthogonality of code sets, leading to decreased target peak power and increased range sidelobes. These issues lower the peak-to-sidelobe ratio, compromising radar performance and reliability.

To tackle these challenges, this thesis presents the following contributions:

1. **Adaptive Block FFT Method:** We propose an adaptive block FFT-based correlator processing method, wherein the blocks are determined based on at least one of the following inputs: initial range computation from the radar, range from another sensor modality, or distance to static obstructions/lane topologies from a digital map. The complexity of traditional correlators is particularly high for large sequence lengths needed for high range and fine velocity resolution. The proposed method significantly reduces complexity by adapting the FFT blocks based on real-time inputs, improving processing efficiency and providing a scalable solution for high-performance radar systems.

2. **Enhanced Frame Design for MIMO Systems:** By analyzing the impact of code diversity [18] on range and Doppler processing, an improved frame design is developed to apply this principle to MIMO systems. . This enhanced frame design not only attenuates sidelobe levels caused by Doppler shift, but also reduceds the set size requirement, making it suitable for large MIMO systems.

These contributions aim to enhance the performance and efficiency of PMCW radar systems, making them more suitable for autonomous driving applications. By improving range processing and mitigating Doppler effects, this work significantly advances the reliability and effectiveness of radar systems for future ADAS-equipped vehicles.

1.5 Thesis outline

Chapter 1 outlines the motivation for the research, and highlights the development of ADAS and the need for enhanced radar systems to meet growing performance demands. It also examines the benefits and challenges of PMCW radar systems.

In Chapter 2, the adaptive block FFT correlation method for PMCW radar systems is introduced, offering a solution to the high computational complexity of traditional FFT-based correlators, thereby improving processing efficiency and maintaining target detection reliability.

Chapter 3 focuses on the mitigation of Doppler-induced range sidelobes through innovative frame design techniques, leveraging code diversity and optimizing sequence set sizes for large MIMO systems.

Finally, Chapter 4 concludes the thesis by summarizing the key findings and contributions, discussing their implications for future research and practical applications, and suggesting further avenues for enhancing radar performance in ADAS.

Proposed Adaptive Block FFT Correlation Method

2

This chapter introduces the adaptive block FFT correlation method for PMCW radar systems, designed to overcome the high complexity of traditional FFT-based correlators. The need for improved correlation methods arises from the significant computational burden associated with large sequence lengths required for high-resolution range and velocity estimation. Traditional methods, with complexity $\mathcal{O}(L_c \log L_c)$, can hinder radar performance due to increased processing time and resource consumption. The proposed adaptive block FFT method aims to reduce complexity, enhance processing efficiency, and ensure reliable target detection in various operational scenarios.

2.1 State-of-the-Art FFT Method

2.1.1 Introduction

In radar systems, range profiles are typically retrieved using a matched filter, which is the conjugated time-reversed version of the transmitted signal, implemented in the digital domain. A matched filter for an entire measurement frame consisting of M periods corresponds to the entire transmitted frame of M pulses. For large M, implementing a matched filter for the entire pulse burst waveform becomes computationally expensive. To address this, a single-pulse matched filter can be used, and the outputs can be combined. This method reduces computational complexity while maintaining accurate range profile retrieval.

To make the subsequent analysis clearer, we assume N_{acc} equal to 1 and the same pulse is repeated M times to produce the slow-time samples needed for Doppler processing in this chapter. By specifying several variables in the general equation of the transmitted baseband signal (Eq.(1.3)), we obtain a more specific form, represented as Eq.(2.1).

$$s_{i,IF}(t) = \sum_{m=0}^{M-1} \sum_{n=0}^{L_c-1} c_n^{(i)} \operatorname{rect}\left(\frac{t - nT_c - mT_r}{T_c}\right) \quad t \in [0, MT_r) \tag{2.1}$$

After digitization with sampling interval T_c, the sampled transmitted baseband signal is denoted as $s_{i,IF}[n,m]$ which corresponds to $c_n^{(i)}$, and the sampled received signal is represented as $y_j[n,m]$. Considering the duration between two consecutive pulses is equal to T_r, for every multiple of T_r, the last L_c samples of the received signal are compared to delayed copies of the transmitted pseudorandom code sequence.

2.1.2 Correlation in the Time Domain

The principle of correlation in the time domain for range estimation involves analyzing the sampled received baseband signal $y_j[n, m]$ from the j-th receiver. This received signal is an amplitude-scaled and time-delayed version of the transmitted signal, where the time delay corresponds to the range of the target. To estimate this range, we correlate the sampled received signal $y_j[n, m]$ with delayed copies of the transmitted pseudorandom code sequence. For concise expression, we omit m here and directly explain the correlation with $y_j[n]$

The time delay τ represents the propagation delay of the signal from the transmitter to the receiver. By shifting the locally generated code forward in time and searching through different values of τ, we align the received signal with the transmitted signal. The result of this correlation process, known as the range profile, is quantified as:

$$\begin{aligned} r_{i,j}[\tau] &= \sum_{n=0}^{L_c-1} y_j[n] s_i[n-\tau] \\ &= \sum_{n=0}^{L_c-1} y_j[n] c^{(i)}_{(n-\tau)\%L_c} \end{aligned} \tag{2.2}$$

where $j \in \{1, 2, \ldots, N_{rx}\}$, $i \in \{1, 2, \ldots, N_{tx}\}$, and τ represents the range bin index. Since the sequence is periodic, we just use $c^{(i)}_{n-\tau}$ later for simplicity. The range profile $r_{i,j}[\tau]$ is high when the received signal and the delayed code sequence align well, indicating the presence of the desired signal. Conversely, it is low when the signals do not align, typically indicating noise or other interfering signals. By identifying the peaks in the correlation output $r_{i,j}[\tau]$, we can accurately estimate the time delay τ and, subsequently, the target range. This method, while reducing computational complexity compared to full-frame correlation, still operates in the time domain with a complexity of $\mathcal{O}(L_c^2)$.

2.1.3 Correlation in the Frequency Domain

To further reduce complexity, range profiles can be computed in the frequency domain. This is achieved by performing correlation through multiplication of the Fourier transforms of the received signal and the complex conjugate of the transmitted signal. An inverse FFT is then applied to obtain the range profile. The corresponding block diagram is illustrated in Figure 2.1.

The range profile $r_{i,j}[\tau]$ is obtained as follows:

1. **Fourier Transform of Signals**: Compute the Fourier transform of the received signal $y_j[n]$ and the transmitted one $s_i[n]$.

$$Y_j[k] = \sum_{n=0}^{L_c-1} y_j[n] e^{-j\frac{2\pi}{L_c}kn} \tag{2.3}$$

$$S_i[k] = \sum_{n=0}^{L_c-1} s_i[n] e^{-j\frac{2\pi}{L_c}kn} \tag{2.4}$$

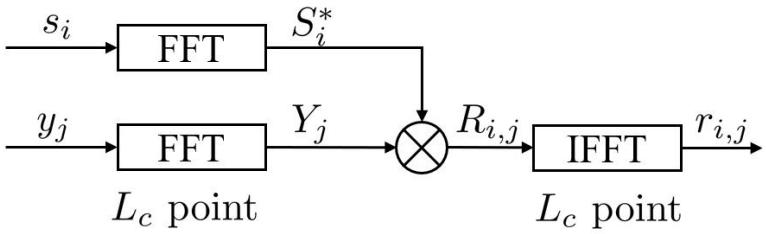

Figure 2.1: Block diagram of FFT-based correlation computation.

2. **Correlation in Frequency Domain:** Multiply the Fourier transform of the received signal by the complex conjugate of the Fourier transform of the transmitted signal.

$$\begin{aligned} R_{i,j}[k] &= Y_j[k]S_i^*[k] \\ &= \sum_{n=0}^{L_c-1} y_j[n]e^{-j\frac{2\pi}{L_c}kn} \sum_{\tau=0}^{L_c-1} s_i[\tau]e^{j\frac{2\pi}{L_c}k\tau} \\ &= \sum_{n=0}^{L_c-1} y_j[n]e^{-j\frac{2\pi}{L_c}kn} \sum_{\tau=0}^{L_c-1} s_i[n-\tau]e^{j\frac{2\pi}{L_c}k(n-\tau)} \\ &= \sum_{\tau=0}^{L_c-1}\sum_{n=0}^{L_c-1} y_j[\tau]s_i[\tau-n]e^{-j\frac{2\pi}{L_c}k\tau} \\ &= \sum_{\tau=0}^{L_c-1} r_{i,j}[\tau]e^{-j\frac{2\pi}{L_c}k\tau} \end{aligned} \tag{2.5}$$

This transformation is possible because of periodic nature of the sequences.

3. **Apply Inverse FFT to Obtain Range Profile**: Finally, perform the inverse FFT on $R_{i,j}[k]$ to obtain the range profile $r_{i,j}[\tau]$

$$r_{i,j}[\tau] = \sum_{k=0}^{L_c-1} R_{i,j}[k]e^{j\frac{2\pi}{L_c}k\tau} \tag{2.6}$$

This method leverages the computational efficiency of FFT, thereby reducing the overall complexity of the range estimation process. Consequently, the complexity for computing range profiles is $\mathcal{O}(L_c \log L_c)$, which is significantly lower compared to time-domain correlation.

2.1.4 Complexity Analysis

Following the schematic overview shown in Figure 1.2, the correlation result then will be coherently accumulated N_acc times and then will undergo Doppler processing to estimate the velocity. By performing a FFT on the phase differences of M pulses, Doppler frequency shifts between successive pulses are extracted, enabling accurate

velocity measurements. The complexity of velocity processing is related to the result of range processing as well, so we calculate the number of additions and multiplications needed for range and Doppler processing for a $N_{tx} \times N_{rx}$ MIMO PMCW radar system (the overview is shown in Figure 2.2).

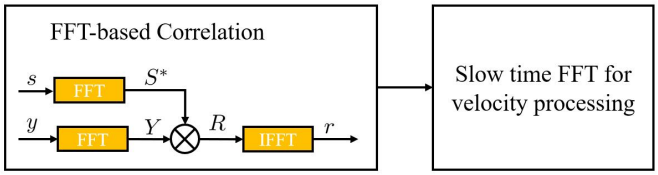

Figure 2.2: Overview of range and velocity processing, with range processing performed using FFT-based correlation.

An N-point FFT requires $\frac{N}{2} \log N$ complex multiplications and $N \log N$ complex additions [32], and a complex multiplication requires 4 real multiplications and 2 real additions, and a complex addition requires 2 real additions. The complexity of range processing and velocity processing will be analyzed separately as follows.

- **Range processing**

Based on the block diagram, we know it takes two L_c-point FFTs and one L_c-point IFFT to obtain $r[\tau]$ for $\tau = 0, 1, \cdots, L_c - 1$. Since the FFTs of the local code could be precomputed and stored in memory, we only consider the complexity of calculating L_c-point FFT to get $Y[k]$, multiplying $Y[k]$ and $S^*[k]$ in frequency domain, and doing L_c-point IFFT. The exact number of real multiplications and additions of doing range processing for $N_{tx} \times N_{rx}$ radar system is shown in Table 2.1.

- **Velocity processing**

Doppler processing is performed after range processing, using a Fast Fourier Transform (FFT) along the slow time axis m. The Doppler processor coherently processes consecutive correlated periods to estimate target velocities. By performing a FFT on the phase differences of M pulses, Doppler frequency shifts between successive pulses are extracted, enabling accurate velocity measurements. The detailed mathematical expression for this process is provided in Chapter 3. Here, we just need to clarify the complexity of doing velocity processing, it takes L_c M-point FFTs for a SISO system, and the exact number of real multiplications and additions of doing velocity processing for $N_{tx} \times N_{rx}$ radar system is also shown in the table below.

2.2 Adaptive Block FFT Correlation Method

In this section, we introduce an innovative adaptive block FFT-based correlator processing method for PMCW radar systems. Traditional FFT-based correlators, while effective, often suffer from high computational complexity, particularly when handling

Table 2.1: Comparison of Computational Complexity for Range and Velocity Processing

Range Processing	
# real Multiplications	$2(N_{rx} + N_{tx}N_{rx})ML_c \log_2 L_c + 4N_{tx}N_{rx}ML_c$
# real Additions	$3(N_{rx} + N_{tx}N_{rx})ML_c \log_2 L_c + 2N_{tx}N_{rx}ML_c$
Velocity Processing	
# real Multiplications	$2N_{tx}N_{rx}ML_c \log_2 M$
# real Additions	$3N_{tx}N_{rx}ML_c \log_2 M$

large sequence lengths necessary for high-resolution range and velocity estimation. To address this, our proposed method dynamically determines the processing blocks based on several inputs, such as initial range computations from the radar, range data from other sensor modalities, or distances to static obstructions and lane topologies derived from digital maps. By adapting the FFT blocks in real-time, this method significantly reduces computational complexity compared to conventional FFT-based correlator processing, enhancing processing efficiency and scalability. In the following sections, we will delve into the principle of the adaptive block FFT-based method, provide a detailed complexity comparison, and present simulation results to demonstrate its effectiveness.

2.2.1 Motivation of Adaptive Block FFT-Based Correlation Method

The motivation behind the adaptive block FFT-based correlation method is to optimize processing by focusing only on the range bins of interest, thereby significantly reducing computational complexity. The range bins of interest are determined based on one of the following inputs: an initial range computation from the radar, range data from another sensor modality such as a LIDAR image, or distances to static obstructions and lane topologies from a digital map.

For instance, an initial range computation from the radar (see Figure 2.3, left) could help determine that targets of interest are within the first quarter of the range bins. Similarly, a LIDAR point cloud image highlighting detected objects at various distances, such as a pedestrian located 50 meters away (see Figure 2.3, middle), can identify specific range bins of interest. Additionally, using useful lane topologies from a digital map, such as T-junctions and bends (see Figure 2.3, right), can further refine the range bins that need to be processed. This targeted approach ensures that only necessary data is processed, thereby reducing computational requirements and enhancing efficiency.

2.2.2 Overview of Adaptive Block FFT-Based Correlation

The adaptive block FFT-based correlator processing method aims to optimize radar signal processing by focusing on the range bins of interest, thereby significantly reducing computational complexity. This method is divided into two main components: adaptive determination of processing blocks and the block FFT-based correlation. As stated before, the complexity of velocity processing is also related to the result of range processing, we include Doppler processing into consideration for comparing the com-

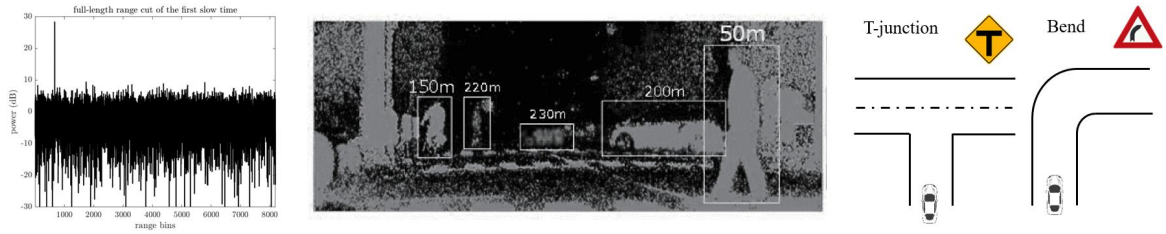

Figure 2.3: Examples of inputs for the adaptive block FFT-based correlation method.Left: Initial range computation from the radar; Middle: LIDAR point cloud image [1] highlighting detected objects at various distances; Right: Map inputs highlighting areas of interest such as T-junctions and bends.

plexity. The whole flowchart provideing an overview of range and velocity processing is shown in Figure 2.4, with range processing performed using adaptive block FFT-based correlation.

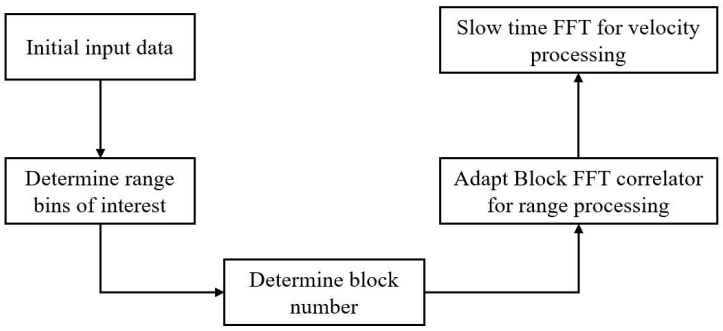

Figure 2.4: Overview of range and velocity processing, with range processing performed using adaptive block FFT-based correlation.

- **Adaptive Determination of Processing Blocks**: The first part of the method involves adaptively determining the block number based on real-time inputs. The initial input data could include an initial range profile from radar, data from other sensor modalities, and information from digital maps regarding static obstructions and lane topology. For example, an initial FFT correlator might provide a preliminary range profile to identify the range bins of interest. Based on this information, we can determine the block number for subsequent correlation, ensuring that only the relevant portions of the signal are processed. This process allows for dynamic adjustment of the block number based on the current situation, potentially changing it for consecutive frames.
- **Block FFT-Based Correlation**: Once the blocks are determined, the method proceeds with the block FFT-based correlation. The identified range bins are processed using the block FFT correlator, which efficiently handles the data by focusing computational resources on the most relevant segments. This approach

allows the system to manage large data sets more effectively, enhancing processing efficiency and scalability.

- **Velocity Processing**: After the block FFT-based correlation, the processed range bins undergo slow-time FFTs to estimate the target velocity.

2.2.3 Methodology of Adaptive Determination of Processing Blocks

The adaptive determination of processing blocks in radar systems is essential for efficiently identifying range bins of interest. The primary objective of this methodology is to ensure that only the relevant portions of the signal are processed, optimizing processing resources and enhancing target detection accuracy. This subsection focuses on the methodology using initial range computations from the radar.

- **How does it work?**

Although different inputs can be used, we here explain the method for the case an initial range profile is computed.

1. **Initial Range Processing**: Perform range processing on the first slow-time period to obtain an initial range profile.
2. **Select an Appropriate Threshold to Detect Peaks**: Utilize a noise power-dependent threshold detector, such as the Constant False Alarm Rate (CFAR) algorithm, to estimate the relevant range bins where targets are likely to be present. This approach ensures that the detection threshold adapts dynamically to varying noise levels, effectively identifying significant peaks corresponding to potential targets.
3. **Determine Range Bins of Interest**: Find the maximum range index among the identified peaks. Add a relaxation margin around this index to define the range bins of interest. Use these identified range bins for processing in the subsequent $M - 1$ slow-time periods.
4. **Subsequent Frames**: At the start of each new frame, the process of determining range bins begins afresh. This approach adapts to changes in the target environment, ensuring that the processed data remains relevant and accurate by focusing on the initial period of each new frame.

- **Why does it work?**

The effectiveness of this adaptive method relies on the minimal displacement of targets over the measurement time frame. Utilizing an 8191-length Gold sequence with a 1 ns chip duration and organizing data into frames of 2048 pulses results in a frame duration $T_{\text{frame}} = M \cdot T_r = M \cdot L_c \cdot T_c = 0.0168$ seconds. Even with a target velocity of 50 m/s, the maximum displacement in range during T_{frame} is $v \cdot T_{\text{frame}} \approx 0.84$ meters.

Given the range resolution $\Delta R = \frac{cT_c}{2} = 0.15$ meters, the displacement in range during T_{frame} corresponds to approximately 6 bins. This rationale supports our approach

to identify the range bins of interest based on initial periods and maintaining this focus in subsequent periods in one frame time.

Therefore, leveraging the initial slow-time data to determine the range bins of interest for the subsequent $M-1$ periods proves effective. This method capitalizes on the limited movement of even swiftly moving targets during a single measurement frame, ensuring that processing remains centered on pertinent range bins. This approach enhances both operational efficiency and the accuracy of target detection.

2.2.4 Methodology of Block FFT-Based Correlation

In this section, we outline the block FFT-based correlation methodology, which improves the efficiency and accuracy of processing large radar signal sequences. such an idea has been proposed in GNSS signal processing [33]. By dividing the computation into manageable segments and using the FFT and IFFT, this approach optimizes computational performance. Here, for clarity of writing, we omit the subscript j and i. An overview is shown in Figure 2.5, which will be explained in detail below.

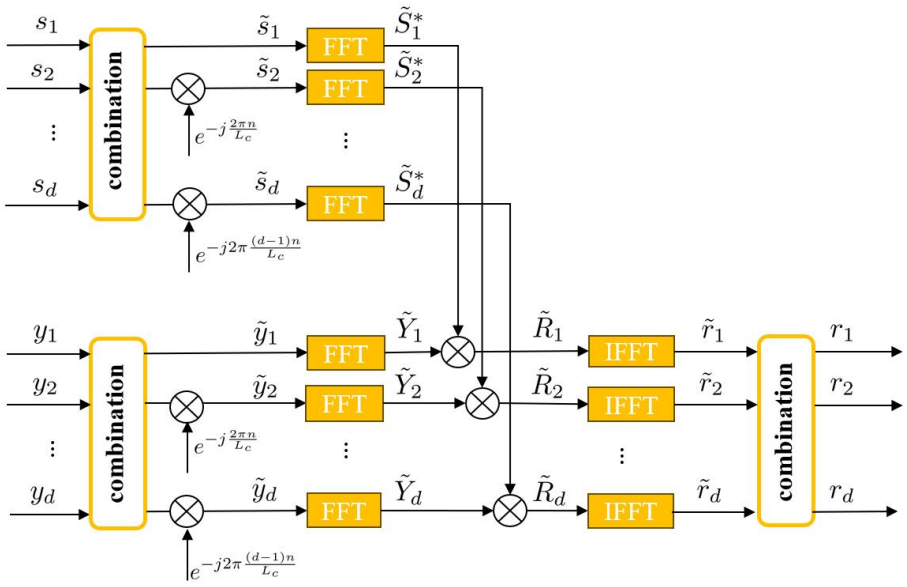

Figure 2.5: Overview of block FFT-based correlator

We firstly split received sampled signal $y[n]$ into d segments which can be expressed as follows:

$$
\begin{aligned}
y_1[n] &= y[n] && \text{for } n = 0, 1, \cdots, \frac{L_c}{d} - 1, \\
y_2[n] &= y[n + \frac{L_c}{d}] && \text{for } n = 0, 1, \cdots, \frac{L_c}{d} - 1, \\
&\vdots \\
y_d[n] &= y[n + (d-1)\frac{L_c}{d}] && \text{for } n = 0, 1, \cdots, \frac{L_c}{d} - 1.
\end{aligned}
$$

Each segment $y_k[n]$ has a local index n ranging from 0 to $\frac{L_c}{d}-1$. The same segmentation method is applied to the sampled transmitted signal $s[n]$ to divide it into d parts.

- **Computation of an FFT of L_c points using d FFTs of $\frac{L_c}{d}$ points**

Let us focus on Eq.(2.3) and write it with segmented parts instead.

$$\begin{aligned}
Y[k] &= \sum_{n=0}^{L_c-1} y[n]e^{-j\frac{2\pi}{L_c}kn} \\
&= \sum_{n=0}^{\frac{L_c}{d}-1} y[n]e^{-j\frac{2\pi}{L_c}kn} + \sum_{n=\frac{L_c}{d}}^{\frac{2L_c}{d}-1} y[n]e^{-j\frac{2\pi}{L_c}kn} + \cdots + \sum_{n=(d-1)\frac{L_c}{d}}^{L_c-1} y[n]e^{-j\frac{2\pi}{L_c}kn} \\
&= \sum_{n=0}^{\frac{L_c}{d}-1} (y_1[n] + y_2[n]e^{-j\frac{2\pi k}{d}} + \cdots + y_d[n]e^{-j\frac{2\pi k(d-1)}{d}})e^{-j\frac{2\pi}{L_c}kn}
\end{aligned}$$

We then down-sample $Y[k]$ by a factor d, and this leads to :

$$\begin{aligned}
\tilde{Y}_1[k] &= Y[dk] \\
&= \sum_{n=0}^{\frac{L_c}{d}-1} (y_1[n] + y_2[n]e^{-j\frac{2\pi dk}{d}} + \cdots + y_d[n]e^{-j\frac{2\pi dk(d-1)}{d}})e^{-j\frac{2\pi}{L_c}dkn} \\
&= \sum_{n=0}^{\frac{L_c}{d}-1} (y_1[n] + y_2[n] + \cdots + y_d[n])e^{-j\frac{2\pi}{L_c/d}kn} \\
&= \sum_{n=0}^{\frac{L_c}{d}-1} \tilde{y}_1[n]e^{-j\frac{2\pi}{L_c/d}kn} \qquad \text{for} \quad k = 0, 1, \ldots, \frac{L_c}{d} - 1 \\
\tilde{Y}_2[k] &= Y[dk+1] \\
&= \sum_{n=0}^{\frac{L_c}{d}-1} \left(y_1[n] + y_2[n]e^{-j\frac{2\pi}{d}} + \cdots + y_d[n]e^{-j\frac{2\pi(d-1)}{d}}\right) e^{-j2\pi\frac{n}{L_c}} e^{-j2\pi\frac{kn}{L_c/d}} \\
&= \sum_{n=0}^{\frac{L_c}{d}-1} \tilde{y}_2[n]e^{-j\frac{2\pi}{L_c/d}kn} \qquad \text{for} \quad k = 0, 1, \ldots, \frac{L_c}{d} - 1 \\
&\vdots \\
\tilde{Y}_d[k] &= Y[dk+d-1] \\
&= \sum_{n=0}^{\frac{L_c}{d}-1} \left(y_1[n] + y_2[n]e^{-j\frac{2\pi(d-1)}{d}} + \cdots + y_d[n]e^{-j\frac{2\pi(d-1)^2}{d}}\right) e^{-j2\pi\frac{(d-1)n}{L_c}} e^{-j2\pi\frac{kn}{L_c/d}} \\
&= \sum_{n=0}^{\frac{L_c}{d}-1} \tilde{y}_d[n]e^{-j\frac{2\pi}{L_c/d}kn} \qquad \text{for} \quad k = 0, 1, \ldots, \frac{L_c}{d} - 1
\end{aligned}$$

Therefore, an L_c-point FFT can be computed using d $\frac{L_c}{d}$-point FFTs, as shown in Figure 2.6, where the combination block includes the elements to compute the operation in parentheses in equation. Computing the FFT of the code sequences, denoted as $S[k]$, can be done in a similar way.

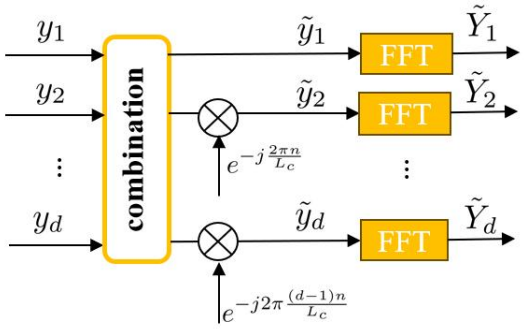

Figure 2.6: Computation of an FFT of L_c points using d FFTs of $\frac{L_c}{d}$ points

- **Multiplication in the frequency domain**

Then, we multiply the conjugate version of $\tilde{S}_d$ with the corresponding $\tilde{Y}_{j,d}$, and we then get d correlation results in the frequency domain.

$$\begin{aligned}
\tilde{R}_1[k] &= \tilde{Y}_1[k]\tilde{S}_1^*[k] \\
\tilde{R}_2[k] &= \tilde{Y}_2[k]\tilde{S}_2^*[k] \\
&\vdots \\
\tilde{R}_d[k] &= \tilde{Y}_d[k]\tilde{S}_d^*[k]
\end{aligned}$$

- **Computation of L_c-point IFFT using d $\frac{L_c}{d}$-point IFFTs**

We start from splitting $r[\tau]$ into d segments as follows:

$$\begin{aligned}
r_1[\tau] &= r[\tau] && \text{for } \tau = 0, 1, \cdots, \frac{L_c}{d} - 1, \\
r_2[\tau] &= r[\tau + \frac{L_c}{d}] && \text{for } \tau = 0, 1, \cdots, \frac{L_c}{d} - 1, \\
&\vdots \\
r_d[\tau] &= r[\tau + (d-1)\frac{L_c}{d}] && \text{for } \tau = 0, 1, \cdots, \frac{L_c}{d} - 1.
\end{aligned}$$

Therefore, the correlation result in the frequency domain $R[k]$ could be given by:

$$
\begin{aligned}
R[k] &= \sum_{\tau=0}^{L_c-1} r[\tau]e^{-j\frac{2\pi}{L_c}k\tau} \\
&= \sum_{\tau=0}^{\frac{L_c}{d}-1} r[\tau]e^{-j\frac{2\pi}{L_c}k\tau} + \sum_{\tau=\frac{L_c}{d}}^{\frac{2L_c}{d}-1} r[\tau]e^{-j\frac{2\pi}{L_c}k\tau} + \cdots + \sum_{\tau=(d-1)\frac{L_c}{d}}^{L_c-1} r[\tau]e^{-j\frac{2\pi}{L_c}k\tau} \\
&= \sum_{\tau=0}^{\frac{L_c}{d}-1} (r_1[\tau] + r_2[\tau]e^{-j\frac{2\pi k}{d}} + \cdots + r_d[\tau]e^{-j\frac{2\pi k(d-1)}{d}})e^{-j\frac{2\pi}{L_c}k\tau}
\end{aligned}
$$

We then down-sample $R[k]$ by a factor d, and this leads to:

$$
\begin{aligned}
\tilde{R}_1[k] &= R[dk] \\
&= \sum_{\tau=0}^{\frac{L_c}{d}-1} (r_1[\tau] + r_2[\tau] + \cdots + r_d[\tau])e^{-j\frac{2\pi}{L_c/d}k\tau} \\
&= \sum_{\tau=0}^{\frac{L_c}{d}-1} \tilde{r}_1[\tau]e^{-j\frac{2\pi}{L_c/d}k\tau} \\
\tilde{R}_2[k] &= R[dk+1] \\
&= \sum_{\tau=0}^{\frac{L_c}{d}-1} (r_1[\tau] + r_2[\tau]e^{-j\frac{2\pi}{d}} + \cdots + r_d[\tau]e^{-j\frac{2\pi(d-1)}{d}})e^{-j2\pi\frac{\tau}{L_c}}e^{-j\frac{2\pi}{L_c/d}k\tau} \\
&= \sum_{\tau=0}^{\frac{L_c}{d}-1} \tilde{r}_2[\tau]e^{-j\frac{2\pi}{L_c/d}k\tau} \\
&\vdots \\
\tilde{R}_d[k] &= R[dk+d-1] \\
&= \sum_{\tau=0}^{\frac{L_c}{d}-1} (r_1[\tau] + r_2[\tau]e^{-j\frac{2\pi(d-1)}{d}} + \cdots + r_d[\tau]e^{-j\frac{2\pi(d-1)^2}{d}})e^{-j2\pi\frac{(d-1)\tau}{L_c}}e^{-j\frac{2\pi}{L_c/d}k\tau} \\
&= \sum_{\tau=0}^{\frac{L_c}{d}-1} \tilde{r}_d[\tau]e^{-j\frac{2\pi}{L_c/d}k\tau}
\end{aligned}
$$

Then we could retrieve $r_1[\tau]$, $r_2[\tau]$ and $r_d[\tau]$ for $\tau = 0, 1, 2, \cdots, \frac{L_c}{d} - 1$.

$$
\begin{aligned}
r_1[\tau] &= \frac{1}{d}\left(\tilde{r}_1[\tau] + \tilde{r}_2[\tau]e^{j\frac{2\pi\tau}{L_c}} + \cdots + \tilde{r}_d[\tau]e^{j\frac{2\pi(d-1)\tau}{L_c}}\right) \\
r_2[\tau] &= \frac{1}{d}\left(\tilde{r}_1[\tau] + \tilde{r}_2[\tau]e^{j\frac{2\pi\tau}{L_c}}e^{j\frac{2\pi}{d}} + \cdots + \tilde{r}_d[\tau]e^{j\frac{2\pi\tau}{L_c}}e^{j\frac{2\pi(d-1)}{d}}\right) \\
&\vdots \\
r_d[\tau] &= \frac{1}{d}\left(\tilde{r}_1[\tau] + \tilde{r}_2[\tau]e^{j\frac{2\pi\tau}{L_c}}e^{j\frac{2\pi(d-1)}{d}} + \cdots + \tilde{r}_d[\tau]e^{j\frac{2\pi\tau}{L_c}}e^{j\frac{2\pi(d-1)^2}{d}}\right)
\end{aligned}
$$

To conclude, the full-length correlation result $r[n]$ can be computed using d $\frac{L_c}{d}$-point IFFTs, as shown in Figure 2.7. The combination block encompasses the elements required to perform the operations within the parentheses of the equation. From the resulting data, we can select one desired segment of length $\frac{L_c}{d}$ that includes our target as the output instead of calculating the whole length correlation result.

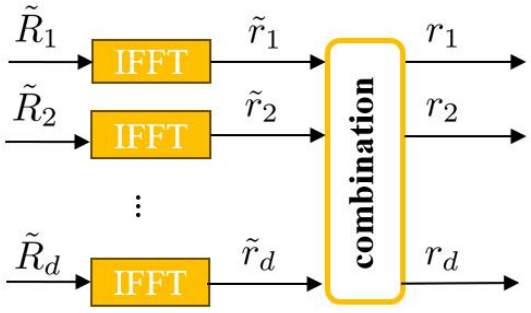

Figure 2.7: Computation of L_c-point IFFT using d $\frac{L_c}{d}$-point IFFTs

2.2.5 Illustrative Example

In this section, we provide a detailed example illustrating the adaptive block FFT method step-by-step. Based on the flowchart shown in Figure 2.4, the detailed description of each step is as follows:

- **Initial FFT correlator**: Perform normal range processing for the first pulse of the frame time, and the initial range cut is shown as in Figure 2.8.
- **Determine range bins of interest**: Use a noise power-dependent threshold detector to estimate the relevant bins of interest where targets may be present. In this example, a target is detected in bin 669.
- **Determine block number**: Considering the range bins of interest with some relaxation, it is within the first $\frac{L_c}{4}$bins. Therefore, we choose the block number d as 4 and focus on the first block result, which is sufficient for subsequent fast-time range correlations.

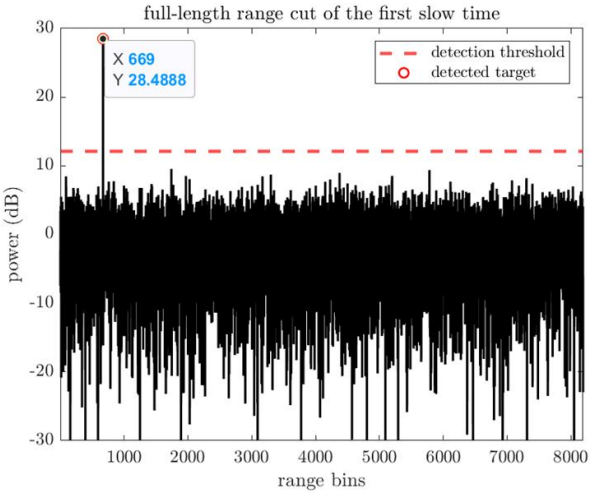

Figure 2.8: Range map with detected target in bin 669.

- **Adapt Block FFT correlator for range processing**: An illustration of the block FFT correlator for $d = 4$ is shown in Figure 2.9. The range correlation result is shown in Figure 2.10

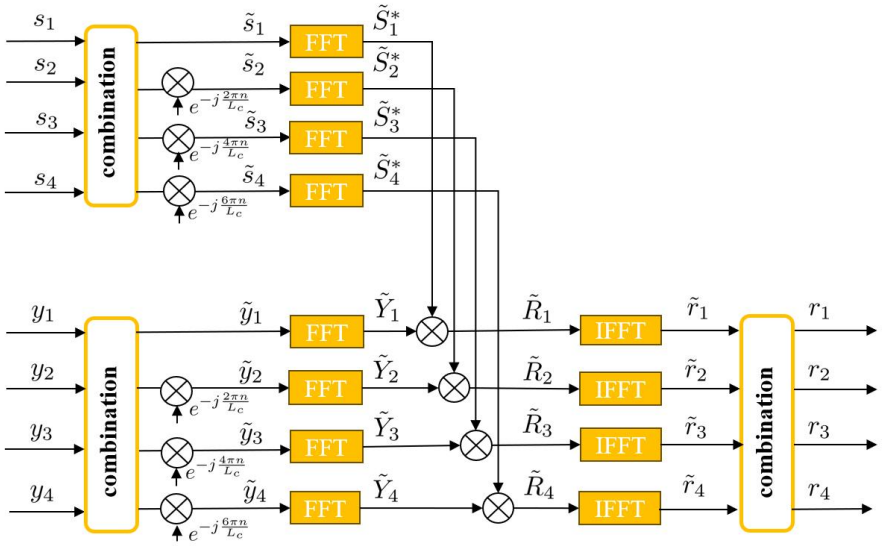

Figure 2.9: Illustration of block FFT-based correlator (d=4)

- **Slow time FFT for velocity processing**: We then do Doppler processing to the data within the desired range bins, the result is shown in Figure 2.11 .

This detailed example demonstrates the adaptive block FFT method, showcasing the step-by-step process of range and Doppler processing in our proposed radar system.

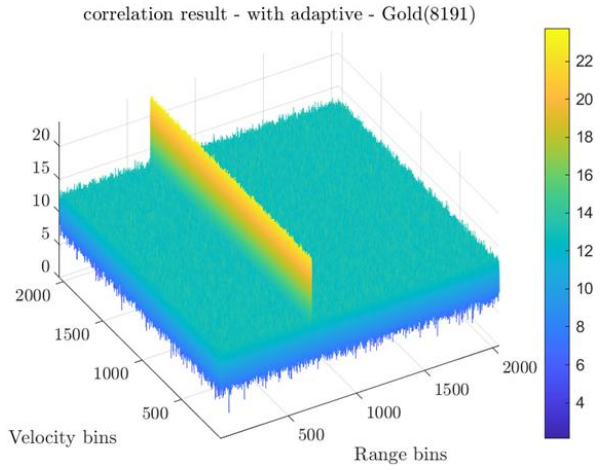

Figure 2.10: Range correlation result within the first $\frac{L_c}{4}$ range bins

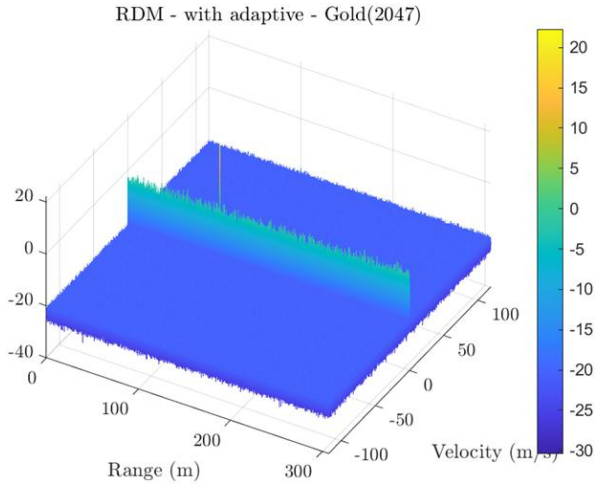

Figure 2.11: Range and Doppler map

2.3 Complexity Comparison

As previously mentioned, the complexity of velocity processing is closely tied to the results of range processing. Therefore, to provide a comprehensive comparison, we evaluate the computational complexity of both FFT-based and block FFT-based correlators by calculating the number of real additions and multiplications required for range and Doppler processing. The computational complexity for the FFT-based correlator is detailed in Table 2.1, while the complexity for the block FFT-based correlator is presented in Table 2.2.

Based on the Figure 2.5, combination step in the block FFT-based correlator involves approximately $dN_{rx}ML_c$ complex multiplications and additions. The element-wise multiplication requires an additional $(d-1)N_{rx}M\frac{L_c}{d}$ complex multiplications. For simplicity, this can be approximated as $N_{rx}ML_c$. The calculation of $\tilde{Y}_1$, $\tilde{Y}_2$, ..., $\tilde{Y}_d$ involves d FFTs of length $\frac{L_c}{d}$, resulting in a requirement of $2N_{rx}ML_c \log_2 \frac{L_c}{d}$ real mul-

Table 2.2: Comparison of computational complexity for range and velocity processing

Range Processing	
# real Multiplications	$2(N_{rx}+N_{tx}N_{rx})ML_c\log_2\frac{L_c}{d}+(8N_{tx}+4d+4)N_{rx}ML_c$
# real Additions	$3(N_{rx}+N_{tx}N_{rx})ML_c\log_2\frac{L_c}{d}+(6N_{tx}+4d+2)N_{rx}ML_c$
Velocity Processing	
# real Multiplications	$2N_{tx}N_{rx}M\frac{L_c}{d}\log_2 M$
# real Additions	$3N_{tx}N_{rx}M\frac{L_c}{d}\log_2 M$

tiplications and $3N_{rx}ML_c\log_2\frac{L_c}{d}$ real additions. To obtain R by multiplying Y and S^*, an additional $N_{tx}N_{rx}ML_c$ complex multiplications are needed, corresponding to $4N_{tx}N_{rx}ML_c$ real multiplications and $2N_{tx}N_{rx}ML_c$ real additions. During the IFFT process, d IFFTs of length $\frac{L_c}{d}$ are computed, necessitating $2N_{tx}N_{rx}ML_c\log_2\frac{L_c}{d}$ real multiplications and $3N_{tx}N_{rx}ML_c\log_2\frac{L_c}{d}$ real additions. The final combination step, involving $d-1$ $\frac{L_c}{d}$-length complex multiplications and additions, sums to $4(d-1)\frac{L_c}{d}N_{tx}N_{rx}M$ real multiplications and real additions. For simplicity, this is extended to $4N_{tx}N_{rx}ML_c$. Consequently, the overall computational complexity for range and Doppler processing using the block FFT-based correlator is summarized in Table 2.2, providing a comprehensive understanding of the processing demands.

There are five variables influencing the overall computational complexity of the radar system. Notably, the complexity is directly proportional to the slow time size M and the code length L_c. For the purpose of comparison, we assume $M = 2048$ and $L_c = 8191$ (padded to 8192 for processing).

We then evaluate the total complexity—including both range and velocity processing—between using FFT-based correlation and block FFT-based correlation for both 4×4 and 8×8 MIMO systems. The results are illustrated in Figure 2.12.

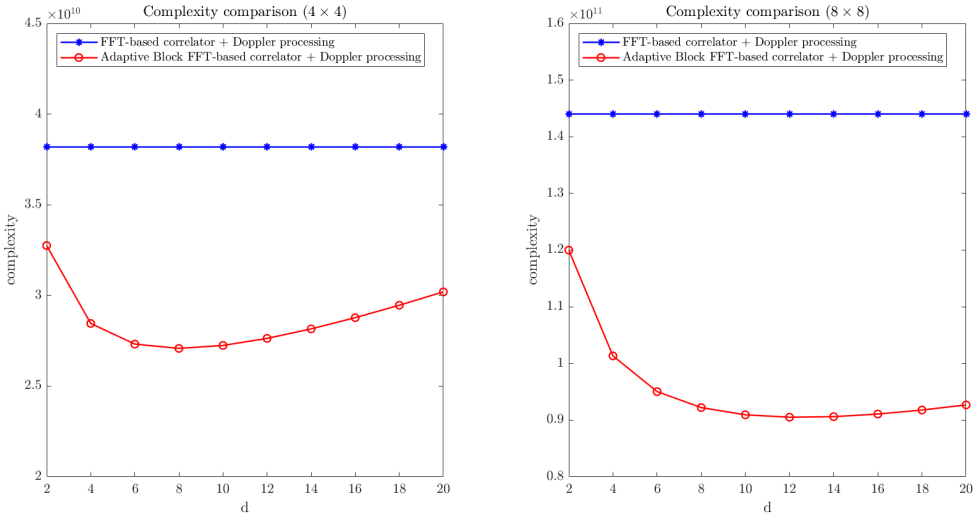

Figure 2.12: Complexity comparison

From this comparison, we observe that in the 4×4 MIMO system, the optimal complexity reduction is achieved at $d = 8$, resulting in approximately a 30% reduction in computational complexity. For the 8×8 MIMO system, the best performance is observed at $d = 12$, yielding a complexity reduction of about 35%. These findings underscore the efficiency gains possible with the appropriate selection of block sizes in block FFT-based correlation.

2.4 Simulation Results

Based on the previous finding, we choose $d = 8$ for the 4×4 MIMO system, and remain the setting $M = 2048$ and $L_c = 8191$. The simulation setup is shown shown in Table 2.3. To verify the effectiveness of the adaptive block FFT-based method for multiple targets, the detailed information of targets are shown in Table 2.4

Table 2.3: Simulation Setup

Simulation Setup	
Number of transmitters (# Tx)	4
Number of receivers (# Rx)	4
Code family	Gold
Code length	8191
Slow time size	2048
Number of accumulations	1

Table 2.4: Target Characteristics

Target	**RCS**	**Distance**	**Velocity**	**DOA**
Target 1	10 dBsm	25 m	10 m/s	0°
Target 2	10 dBsm	50 m	20 m/s	10°
Target 3	10 dBsm	75 m	30 m/s	15°
Target 4	10 dBsm	100 m	40 m/s	-6°
Target 5	10 dBsm	125 m	50 m/s	-11°

To evaluate the methods, we adopt total processing time, peak power and noise floor as performance metrics. The simulation results, comparing the proposed block FFT-based method with the traditional FFT-based method, are shown in Table 2.5. The results indicate that the block FFT-based method significantly reduces the processing times compared to the traditional FFT-based method. This aligns with our previous analysis of computational complexity, demonstrating that the block FFT-based method offers superior efficiency and scalability for advanced radar systems.

Table 2.5: Comparison of processing times

Method	**Total**	**Range**	**Velocity**
FFT-based method	75.152	32.236s	30.068s
Adaptive block FFT-based method	24.128	20.681s	3.048s

The Range and Doppler Map (RDM) comparison between the FFT-based method and the adaptive block FFT-based method is illustrated in Figure 2.13. From the figure, it is evident that applying the adaptive block FFT-based method does not affect the target peak or the noise floor, thus maintaining the Signal-to-Noise Ratio (SNR) at the same level as the FFT-based method. This confirms the effectiveness of the adaptive method in preserving detection performance while reducing computational complexity.

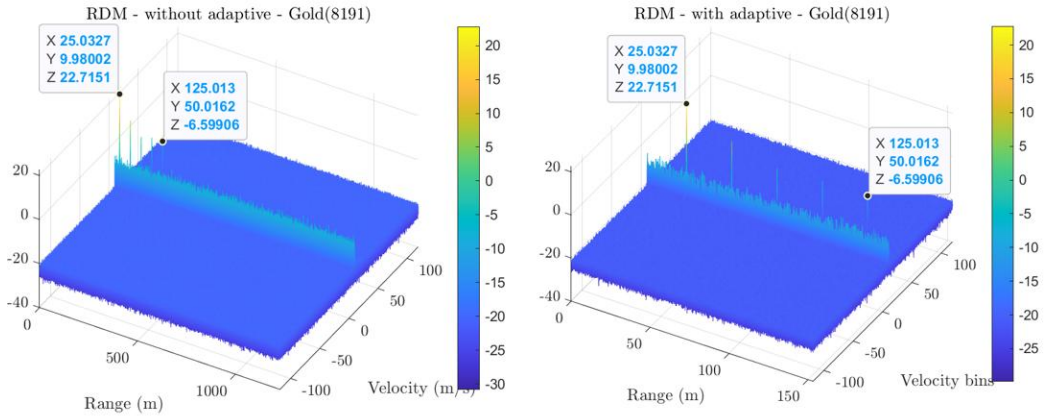

Figure 2.13: RDM Comparison

2.5 Conclusion

In this chapter, we introduced the adaptive block FFT-based correlation method for PMCW radar systems, aimed at addressing the high computational complexity inherent in traditional FFT-based correlators. The need for efficient correlation methods is driven by the substantial computational demands of processing large sequence lengths, which are necessary for achieving high-resolution range and velocity estimation in radar systems. Our proposed method seeks to optimize computational resources, enhance processing efficiency, and ensure reliable target detection across various operational scenarios.

We began by examining the state-of-the-art FFT methods, highlighting their effectiveness in reducing complexity compared to time-domain correlation but also recognizing their limitations in handling large data sets. This provided a foundation for introducing our adaptive block FFT-based method, which leverages dynamic determination of processing blocks to focus on range bins of interest. This targeted approach significantly reduces computational load without compromising accuracy.

The methodology of the adaptive block FFT-based correlation method was detailed in several key components:

1. Adaptive Determination of Processing Blocks: We explained how processing blocks are adaptively determined using inputs such as initial range computations, sensor data, and map information. This step ensures that only relevant data segments are processed, optimizing efficiency.

2. Block FFT-Based Correlation: We outlined the methodology for dividing the FFT computation into manageable blocks, performing FFTs and IFFTs on these segments, and combining the results to obtain the final correlation output. This approach maintains accuracy while reducing computational requirements.

3. Complexity Comparison: We conducted a detailed comparison of the computational complexity between the traditional FFT-based method and our proposed adaptive block FFT-based method. The results showed a significant reduction in complexity, particularly for larger MIMO settings, longer code lengths, and greater slow time sizes.

4. Simulation Results: We provided simulation results to verify the effectiveness of the adaptive block FFT-based method. The results demonstrated substantial reductions in processing time without affecting the target peak or noise floor, confirming that our method maintains the same level of SNR as the traditional FFT-based method.

In conclusion, the adaptive block FFT-based correlation method offers a promising solution for enhancing the efficiency and scalability of PMCW radar systems. By dynamically adapting the processing blocks based on real-time inputs, this method effectively reduces computational complexity while preserving detection performance. These advantages make the adaptive block FFT-based method a valuable approach for advanced radar systems requiring high-resolution range and velocity estimation. Future work may explore further optimizations and extensions of this method to handle even more complex and diverse operational scenarios.

Frame Design to Reduce Doppler-Induced Range Sidelobes

3

In this chapter, we delve into the crucial aspect of frame design aimed at mitigating the range sidelobe effects induced by Doppler shifts. When targets move relative to the radar, the resulting Doppler effect introduces phase shifts in the fast-time domain, significantly reducing the orthogonality of binary codes. This degradation leads to decreased target peak power and increased range sidelobes, ultimately lowering the peak-to-sidelobe ratio. These issues pose a challenge for reliable detection of both large and small targets in automotive radar applications.

Traditional approaches to address this issue involve compensating for the Doppler frequency shift through Fourier analysis and phase adjustment in the fast-time domain. While effective, these methods significantly increase computational complexity and are not always feasible for real-time processing. Alternatively, varying the transmitted code sequence for each slow-time sample (code diverisity frame) offers a low-complexity solution but requires a large family of code sequences with excellent correlation properties, which is particularly demanding for large MIMO systems.

This chapter presents a comprehensive analysis of code diversity frame and introduces enhanced radar frame design techniques for applying it to MIMO systems. By leveraging code diversity and optimizing sequence set sizes, we aim to achieve a balance between sidelobe attenuation and computational efficiency, thereby improving radar performance and reliability in the presence of Doppler shifts.

3.1 Generalized Frame Design Representation

Code Division Multiple Access (CDMA) is a technique widely used in wireless communication and radar systems to enable multiple transmitters to operate simultaneously without significant interference. In the context of Phase Modulated Continuous Wave (PMCW) radar systems, CDMA plays a crucial role in multi-target detection and inter-radar interference resistance. Each transmitter is assigned a unique orthogonal code sequence, allowing the simultaneous transmission of multiple signals on the same frequency band while minimizing cross-correlation. The transmitted signal in PMCW radar is phase-modulated using these assigned code sequences, maintaining signal orthogonality and aiding accurate detection of multiple targets. The frame design for PMCW radar often involves coherent accumulation, where the same code sequence is repeated multiple times to enhance the Signal-to-Noise Ratio (SNR) by coherently summing the received signals, thereby improving radar detection capability. The performance of a radar system is heavily dependent on the auto-correlation and cross-correlation properties of the code sequences; good auto-correlation properties ensure that the main lobe is prominent with minimal sidelobes, while good cross-correlation

properties minimize interference between different transmitters.

3.1.1 Generalized Transmitted Frame Scheme

The generalized transmitted frame scheme for acquiring one radar data cube is illustrated in Figure 3.1. This design involves the following key elements:

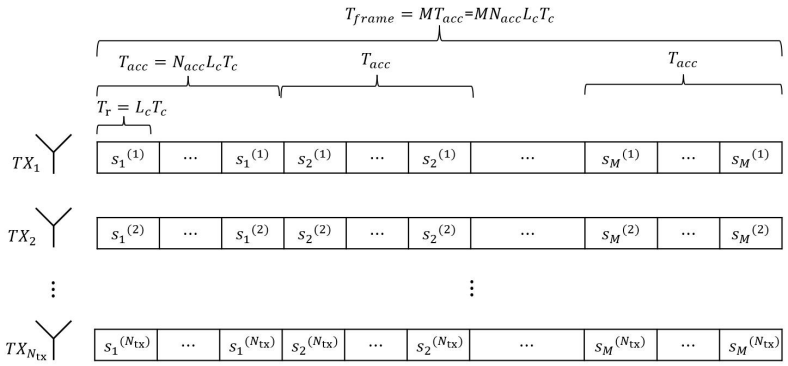

Figure 3.1: Generalized transmitted frame scheme for the acquisition of one radar data cube

- **Code Sequence $s_m^{(i)}$**:
  - For the i_{th} transmitter and m_{th} slow time index, the corresponding code sequence is represented as $s_m^{(i)}$.
  - The duration of one code sequence is $T_r = L_c \cdot T_c$, where T_c is the duration of one chip in the sequence.
- **Coherent Accumulation**:
  - The code sequence is repeated N_{acc} times for coherent accumulation.
  - The accumulation period is $T_{\text{acc}} = N_{\text{acc}} \cdot T_r$.
  - Coherent accumulation helps in increasing the SNR by summing the received signals coherently.
- **Slow-Time Samples for Doppler Processing**:
  - The accumulation period T_{acc} is repeated M times to produce the slow-time samples needed for Doppler processing.
  - This repetition allows capturing temporal variations due to the relative motion of targets, which is essential for Doppler analysis.

3.1.2 Range and Velocity Processing analysis

To make the analysis concise, we assume that is only one target which is represented as (R_0, v_0, θ_0), and then the delay from the transmitter to receiver is $\tau_0(t) = \frac{2(R_0+v_0t)}{c} =$

$\tau_0 + \frac{2v_0}{c}t$. Therefore, based on Eq.(1.5), the received baseband signal of jth receiver is given as:

$$y_j(t) = \tilde{\beta}_0 \phi_{R,\theta_0}^{j-1} \sum_{i=1}^{N_{tx}} \phi_{T,\theta_0}^{i-1} s_{i,IF}(t-\tau_0) e^{j2\pi f_{d,0} t} \tag{3.1}$$

where $\phi_{T,\theta_0} = e^{j2\pi \frac{d_T \sin\theta_0}{\lambda}}$, $\phi_{R,\theta_0} = e^{j2\pi \frac{d_R \sin\theta_0}{\lambda}}$, $f_{d,0} = -f_c \frac{2v_0}{c}$, and the transmitted baseband signal from the i_{th} transmitter is now given as:

$$s_{i,IF}(t) = \sum_{m=0}^{M-1} \sum_{n_{acc}=0}^{N_{acc}-1} \sum_{n=0}^{L_c-1} c_n^{(i,m)} \text{rect}\left(\frac{t - nT_c - n_{acc}T_r - mT_r}{T_c}\right) \quad t \in [0, N_{acc}MT_r) \tag{3.2}$$

After digitization, the time is split into fast time index n with time interval T_c, accumulation index n_{acc} and slow time index m with time interval T_r to estimate the range and the Doppler information. It is given as:

$$t = nT_c + n_{acc}T_r + mT_r \tag{3.3}$$

Assume $\tau_0 = \hat{\tau_0}T_c + \delta_\tau T_c$ with $\hat{\tau_0}$ being an integer and $\delta_\tau \in [-0.5, 0.5)$. The received data are sampled with the sampling interval T_c and we obtain

$$y_j[n, n_{acc}, m] \approx \tilde{\beta}_0 \phi_{R,\theta_0}^{j-1} \sum_{i=1}^{N_{tx}} \phi_{T,\theta_0}^{i-1} c_{n-\hat{\tau_0}}^{(i,m)} e^{j2\pi f_{d,0}(nT_c + n_{acc}T_r + mT_r)} \tag{3.4}$$

- **Range Processing**

As previously mentioned, range processing is performed through correlation. In this context, we focus on the correlation with the code transmitted by the i_{th} transmitter, which represents the auto-correlation part. The same principle applies when considering the correlation with codes from other transmitters. The accumulated correlation can be expressed as follows:

$$\begin{aligned}
r_{i,j}[\tau, m] &= \sum_{n_{acc}=0}^{N_{acc}-1} \sum_{n=0}^{L_c-1} y_j[n, n_{acc}, m] s_i[n-\tau, m] \\
&= \sum_{n_{acc}=0}^{N_{acc}-1} \sum_{n=0}^{L_c-1} \tilde{\beta}_0 \phi_{R,\theta_0}^{j-1} \sum_{i=1}^{N_{tx}} \phi_{T,\theta_0}^{i-1} c_{n-\hat{\tau_0}}^{(i,m)} e^{j2\pi f_{d,0}(nT_c + n_{acc}T_r + mT_r)} s_i[n-\tau, m] \\
&= \sum_{n_{acc}=0}^{N_{acc}-1} \tilde{\beta}_0 \phi_{R,\theta_0}^{j-1} e^{j2\pi f_{d,0}(n_{acc}+m)T_r} \sum_{i=1}^{N_{tx}} \phi_{T,\theta_0}^{i-1} \sum_{n=0}^{L_c-1} c_{n-\hat{\tau_0}}^{(i,m)} e^{j2\pi f_{d,0} nT_c} c_{n-\tau}^{(i,m)} \\
&= \tilde{\beta}_0 \phi_{R,\theta_0}^{j-1} e^{j2\pi f_{d,0} mT_r} \sum_{n_{acc}=0}^{N_{acc}-1} e^{j2\pi f_{d,0} n_{acc} T_r} \sum_{i=1}^{N_{tx}} \phi_{T,\theta_0}^{i-1} \tilde{r}_{i,m}[\tau]
\end{aligned} \tag{3.5}$$

where $\tilde{r}_{i,m}[\tau] = \sum_{n=0}^{L_c-1} c_{n-\hat{\tau_0}}^{(i,m)} e^{j2\pi f_{d,0} nT_c} c_{n-\tau}^{(i,m)}$.

- **Velocity Processing**

Following the schematic overview shown in Figure 1.2, Doppler processing is performed after range processing, which is done via a Discrete Fourier Transform (DFT) along the slow time axis m. Focusing on the desired range bin $\hat{\tau}$, we obtain the DFT result:

$$\begin{aligned}\mathcal{R}_{i,j}[\hat{\tau},k] &= \sum_{m=0}^{M-1} r_{i,j}[\hat{\tau},m]e^{-j\frac{2\pi}{M}mk} \\ &= \sum_{m=0}^{M-1} \tilde{\beta}_0\phi_{R,\theta_0}^{j-1}e^{j2\pi f_{d,0}mT_r}\sum_{n_{acc}=0}^{N_{acc}-1} e^{j2\pi f_{d,0}n_{acc}T_r}\sum_{i=1}^{N_{tx}}\phi_{T,\theta_0}^{i-1}\tilde{r}_{i,m}[\hat{\tau}]e^{-j\frac{2\pi}{M}mk} \\ &= \tilde{\beta}_0\phi_{R,\theta_0}^{j-1}\sum_{n_{acc}=0}^{N_{acc}-1} e^{j2\pi f_{d,0}n_{acc}T_r}\sum_{m=0}^{M-1}\sum_{i=1}^{N_{tx}}\phi_{T,\theta_0}^{i-1}\tilde{r}_{i,m}[\hat{\tau}]e^{j2\pi f_{d,0}mT_r}e^{-j\frac{2\pi}{M}mk}\end{aligned} \tag{3.6}$$

From it, in the frequency distribution of the slow-time domain, the peak appears at the cell $\hat{k_d}$ where $\hat{k_d} = Mf_{d,0}T_r$. Let assume $k = \hat{k_d} + \Delta_k$ with Δ_k being an integer represents the cell diviation from the estimated one. Thus, Eq.(3.6) could be written as

$$\mathcal{R}_{i,j}[\hat{\tau},\Delta_k] = \tilde{\beta}_0\phi_{R,\theta_0}^{j-1}\sum_{n_{acc}=0}^{N_{acc}-1} e^{j2\pi f_{d,0}n_{acc}T_r}\sum_{m=0}^{M-1}\sum_{i=1}^{N_{tx}}\phi_{T,\theta_0}^{i-1}\tilde{r}_{i,m}[\hat{\tau}]e^{-j\frac{2\pi}{M}m\Delta_k} \tag{3.7}$$

3.2 State-of-the-Art Frame Design

The state-of-the-art transmitted frame for acquiring one radar data cube is structured to enhance SNR and maintain code orthogonality, as illustrated in Figure 3.2. This design retains most of the key elements mentioned previously, with a slight modification in the Code Sequence part, described as follows:

- **Code Sequence** $s_m^{(i)}$:
  - Each transmitter uses the same code sequence of length L_c for all slow time index m, which means $s_m^{(i)} = s^{(i)}$.
  - The duration of one code sequence is $T_r = L_c \cdot T_c$, where T_c is the duration of one chip in the sequence.

3.2.1 Analysis of State-of-the-Art Frame Design

We maintain the assumption of a single target, represented by (R_0, v_0, θ_0). Based on the frame scheme, transmitting the same sequence for each transmitter, we have $c_n^{(i,m)} = c_n^{(i)}$.

- **Range Processing**

Here, we still specifically consider the correlation with the code transmitted by the i_{th} transmitter, and we obtain the correlation result

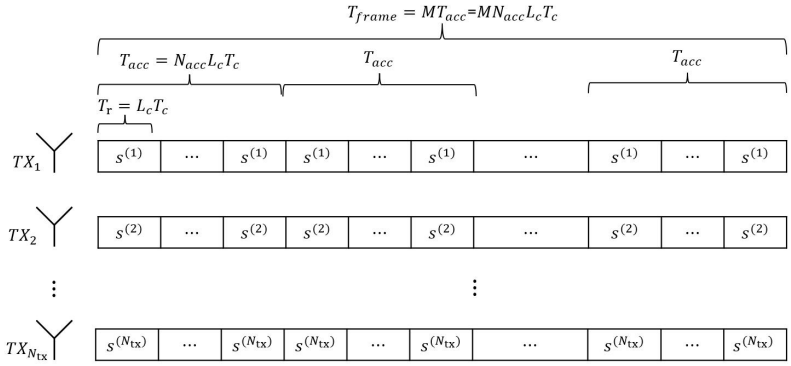

Figure 3.2: State-of-the-Art transmitted frame for the acquisition of one radar data cube

$$
\begin{aligned}
r_{i,j}[\tau, m] &= \sum_{n_{acc}=0}^{N_{acc}-1} \tilde{\beta}_0 \phi_{R,\theta_0}^{j-1} e^{j2\pi f_{d,0}(n_{acc}+m)T_r} \sum_{i=1}^{N_{tx}} \phi_{T,\theta_0}^{i-1} \sum_{n=0}^{L_c-1} c_{n-\hat{\tau_0}}^{(i)} e^{j2\pi f_{d,0} n T_c} c_{n-\tau}^{(i)} \\
&= \tilde{\beta}_0 \phi_{R,\theta_0}^{j-1} e^{j2\pi f_{d,0} m T_r} \sum_{n_{acc}=0}^{N_{acc}-1} e^{j2\pi f_{d,0} n_{acc} T_r} \sum_{i=1}^{N_{tx}} \phi_{T,\theta_0}^{i-1} \tilde{r}_i[\tau]
\end{aligned}
\tag{3.8}
$$

where $\tilde{r}_i[\tau] = \sum_{n=0}^{L_c-1} c_{n-\hat{\tau_0}}^{(i)} e^{j2\pi f_{d,0} n T_c} c_{n-\tau}^{(i)}$ is independent of m. This is the key difference compared to the generalized frame scheme.

- **Velocity Processing**

We still focus on the desired range bin $\hat{\tau}$, and do DFT along the slow time axis m. Based on the same assumption mentioned before, $k = \hat{k_d} + \Delta_k$ where $\hat{k_d} = M f_{d,0} T_r$.

$$
\begin{aligned}
\mathcal{R}_{i,j}[\hat{\tau}, \Delta_k] &= \tilde{\beta}_0 \phi_{R,\theta_0}^{j-1} \sum_{n_{acc}=0}^{N_{acc}-1} e^{j2\pi f_{d,0} n_{acc} T_r} \sum_{m=0}^{M-1} \sum_{i=1}^{N_{tx}} \phi_{T,\theta_0}^{i-1} \tilde{r}_i[\hat{\tau}] e^{-j\frac{2\pi}{M} m \Delta_k} \\
&= \tilde{\beta}_0 \phi_{R,\theta_0}^{j-1} \sum_{n_{acc}=0}^{N_{acc}-1} e^{j2\pi f_{d,0} n_{acc} T_r} \sum_{m=0}^{M-1} e^{-j\frac{2\pi}{M} m \Delta_k} \left(\sum_{i=1}^{N_{tx}} \phi_{T,\theta_0}^{i-1} \tilde{r}_i[\hat{\tau}] \right)
\end{aligned}
\tag{3.9}
$$

- **Analysis**

Note that $\tilde{r}_i[\tau] = \sum_{n=0}^{L_c-1} c_{n-\hat{\tau_0}}^{(i)} e^{j2\pi f_{d,0} n T_c} c_{n-\tau}^{(i)}$, where the term $e^{j2\pi f_{d,0} n T_c}$ introduces a redundant phase shift to the binary code. This phase shift reduces the orthogonality of the codes, resulting in higher sidelobe levels in the range profile. Without any phase adjustment, the performance of the range profile, obtained through correlation, can be significantly degraded, especially in the presence of a high Doppler frequency shift. When calculating $\mathcal{R}_j[\hat{\tau}, \Delta_k]$, the summation over M pulses accumulates $\tilde{r}_i[\tau]$ M times, leading to increased sidelobe levels in the range profile.

Additionally, as shown in Eq.(3.10), the summation $\sum_{m=0}^{M-1} A e^{-j\frac{2\pi}{M} m \Delta_k}$ exhibits a sharp peak when $\Delta_k = 0$, and is zero in other bins. Consequently, the frequency

response is characterized by a single sharp peak, which appears at the cell $\hat{k_d}$. Besides, the response in other bins is null, highlighting the clear distinction in the frequency domain representation.

$$\sum_{m=0}^{M-1} Ae^{-j\frac{2\pi\Delta_k}{M}m} = \begin{cases} AM & \text{if } \Delta_k = 0 \\ A\frac{1-e^{-j\frac{2\pi\Delta_k}{M}M}}{1-e^{-j\frac{2\pi\Delta_k}{M}}} = 0 & \text{if } \Delta_k \neq 0 \end{cases} \tag{3.10}$$

3.2.2 Simulation Result

The simulation setup and target characteristics are outlined in Table 3.1, which will be used to evaluate the state-of-the-art frame design. The resulting Range and Doppler Map (RDM) is shown in Figure 3.3. From it, we observe that the Doppler effects introduce significant sidelobes, and the target appears as a sharp peak in the desired velocity bin. These observations are consistent with the previous analysis.

Table 3.1: Simulation Setup and Target Characteristics

Simulation Setup		**Target Characteristics**	
MIMO: $N_{tx} \times N_{rx}$	8×8	Radar Cross Section	25 dBsm
Slow time size: M	198	Distance: R_q	20 m
Accumulation number: N_{acc}	2	Velocity: v_q	50 m/s
'Gold' code length: L_c	2047	Angular: θ_q	0°

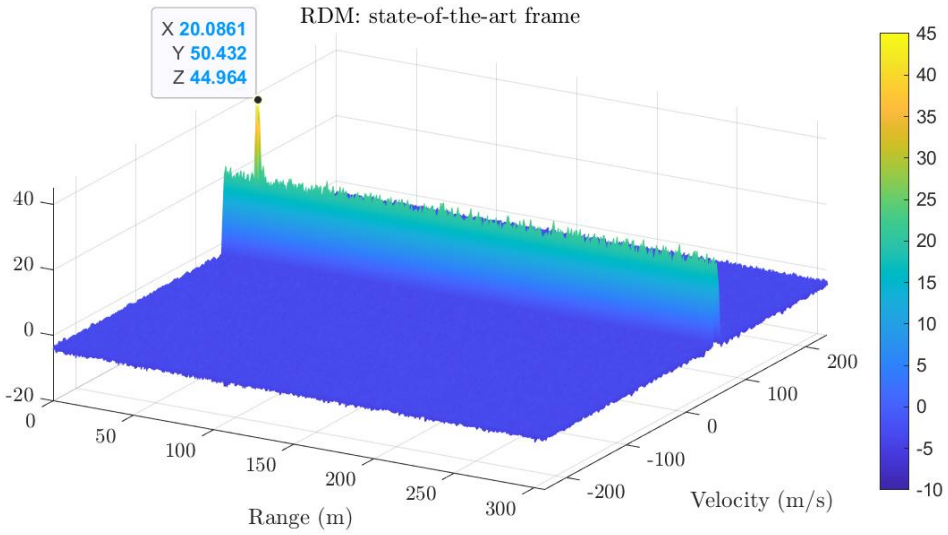

Figure 3.3: RDM utilizing the state-of-the-art frame design

3.3 Code Diversity Frame Design

Instead of transmitting continuously the same sequence, which repeatedly produces identical range sidelobe degradation, the proposed solution is to send a new sequence

at every slow time index [18].

3.3.1 Code Diversity Frame Scheme

The Transmitted frame for the acquisition of one radar data cube with code diversity is the same as the generalized frame scheme shown in Figure 3.1.

Here, we need to exemplify two key different parts, one is related to code sequence and another is related to coherent accumulation.

- **Code Sequence** $s_m^{(i)}$:
  - For the i-th transmitter, it uses a unique code sequence $s_m^{(i)}$ for each accumulation at every slow time index m, with a total of M unique sequences.
  - The duration of one code sequence remains $T_r = T_c L_c$, where T_c is the duration of one chip in the sequence.
- **Coherent Accumulation**:
  - Since the transitions between two different sequences breaks the periodicity of the signal, we need to adjust the coherent accumulation part a little bit. Even if a sequence is repeated N_{acc} times, only the last $N_{acc} - 1$ periods will be used for accumulation because the first period contains very high range sidelobes as the periodicity has been lost.
  - Such a different coherent accumulation would sacrifice at most 3dB peak-to-noise power when it only use one correlation result instead of accumulating 2 results. But the effect of such a sacrifice will decrease with the increase of N_{acc} (doing $N_{acc} - 1$ accumulations instead of N_{acc}). This means the worst case is 3dB peak-to-noise power lost with the code diversity frame scheme. However, the benefit of it exceeds 3dB which will be discussed later.

3.3.2 Range and Velocity Processing analysis

Unlike the state-of-the-art frame design, code divesity frame requires to repeat the code sequence N_{acc} times, and only accumulate on the last $N_{acc} - 1$ samples. Considering the sequence is changed at different slow time indices, the transmitted baseband signal from the ith transmitter $s_{i,IF}(t)$ is given as

$$s_{i,IF}(t) = \sum_{m=0}^{M-1} \sum_{n_{acc}=0}^{N_{acc}-1} \sum_{n=0}^{L_c-1} c_n^{(i,m)} \text{rect}\left(\frac{t - nT_c - n_{acc}T_r - mT_r}{T_c}\right) \quad t \in [0, N_{acc}MT_r) \tag{3.11}$$

- **Range Processing**

Here, we specifically consider the correlation with the code transmitted by the i_{th} transmitter. Discarding the correlation result from the first period, the correlation

result is given as:

$$\begin{aligned} r_{i,j}[\tau, m] &= \sum_{n_{acc}=1}^{N_{acc}-1} \sum_{n=0}^{L_c-1} y_j[n, n_{acc}, m] s_i[n-\tau, m] \\ &= \sum_{n_{acc}=1}^{N_{acc}-1} \sum_{n=0}^{L_c-1} \tilde{\beta}_0 \phi_{R,\theta_0}^{j-1} \sum_{i=1}^{N_{tx}} \phi_{T,\theta_0}^{i-1} c_{n-\hat{\tau_0}}^{(i,m)} e^{j2\pi f_{d,0}(nT_c + n_{acc}T_r + mT_r)} s_i[n-\tau, m] \\ &= \tilde{\beta}_0 \phi_{R,\theta_0}^{j-1} e^{j2\pi f_{d,0} m T_r} \sum_{n_{acc}=1}^{N_{acc}-1} e^{j2\pi f_{d,0} n_{acc} T_r} \sum_{i=1}^{N_{tx}} \phi_{T,\theta_0}^{i-1} \tilde{r}_{i,m}[\tau] \end{aligned} \tag{3.12}$$

where $\tilde{r}_{i,m}[\tau] = \sum_{n=0}^{L_c-1} c_{n-\hat{\tau_0}}^{(i,m)} e^{j2\pi f_{d,0} n T_c} c_{n-\tau}^{(i,m)}$, it is dependent on slow time index m.

- **Velocity Processing**

We still focus on the desired range bin $\hat{\tau}$, and do DFT along the slow time axis m. Based on the same assumption mentioned before, $k = \hat{k_d} + \Delta_k$ and cell $\hat{k_d}$ satisfies $\hat{k_d} = M f_{d,0} T_r$. Thus, we obtain

$$\begin{aligned} \mathcal{R}_{i,j}[\hat{\tau}, \Delta_k] &= \tilde{\beta}_0 \phi_{R,\theta_0}^{j-1} \sum_{n_{acc}=1}^{N_{acc}-1} e^{j2\pi f_{d,0} n_{acc} T_r} \sum_{m=0}^{M-1} \sum_{i=1}^{N_{tx}} \phi_{T,\theta_0}^{i-1} \tilde{r}_{i,m}[\hat{\tau}] e^{-j\frac{2\pi}{M} m \Delta_k} \\ &= \tilde{\beta}_0 \phi_{R,\theta_0}^{j-1} \sum_{n_{acc}=1}^{N_{acc}-1} e^{j2\pi f_{d,0} n_{acc} T_r} \sum_{i=1}^{N_{tx}} \phi_{T,\theta_0}^{i-1} \left(\sum_{m=0}^{M-1} \tilde{r}_{i,m}[\hat{\tau}] e^{-j\frac{2\pi}{M} m \Delta_k} \right) \end{aligned} \tag{3.13}$$

- **Analysis**

Note that $\tilde{r}_{i,m}[\tau] = \sum_{n=0}^{L_c-1} c_{n-\hat{\tau_0}}^{(i,m)} e^{j2\pi f_{d,0} n T_c} c_{n-\tau}^{(i,m)}$, where the term $e^{j2\pi f_{d,0} n T_c}$ introduces a phase shift that affects the binary code. This phase shift can decrease the orthogonality of the codes, resulting in higher sidelobe levels in the range profile. However, this effect is dependent on the slow time index m, meaning the phase shift varies across different pulses. When calculating $\mathcal{R}_j[\hat{\tau}, \Delta_k]$ as shown in Eq.(3.13), the summation over M pulses is introduced. Because the Doppler-induced phase shift affects each sequence differently, summing the pulses together prevents these phase shift effect from aligning constructively, thereby reducing the sidelobe level. The extent of sidelobe attenuation depends on the number of pulses, denoted as M.

Another effect of the dependency of $\tilde{r}_{i,m}[\tau]$ on m is that, unlike in Eq.(3.9), we cannot factor out the term $\sum_{m=0}^{M-1} e^{-j\frac{2\pi}{M} m \Delta_k}$. Consequently, the frequency response no longer exhibits a single sharp peak but instead shows a spreading effect. This spreading indicates a decrease in the ability to coherently sum the signal, which can negatively impact the velocity resolution.

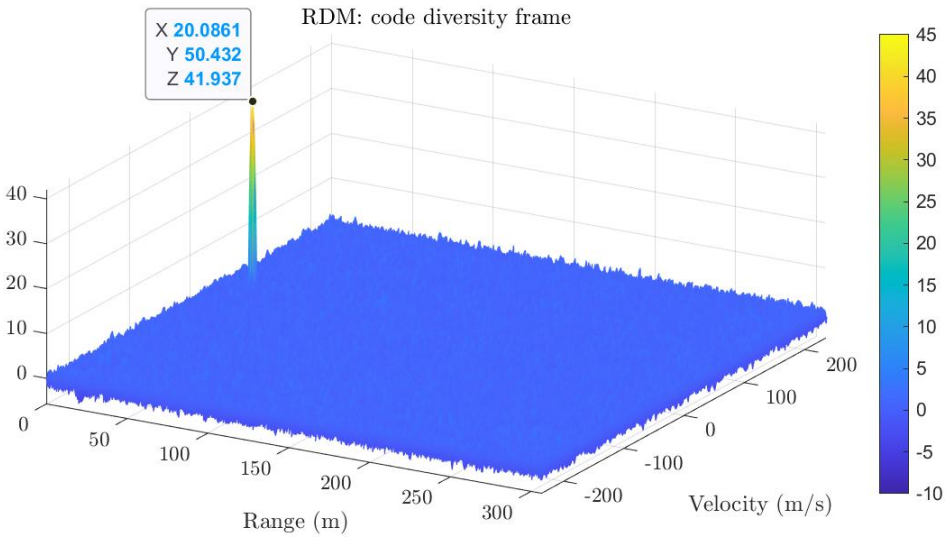

Figure 3.4: RDM utilizing the code diversity frame Design

3.3.3 Simulation Result

We maintain the same simulation setup and target characteristics used in the simulation for the state-of-the-art frame design which is shown in Table 3.1, and the resulting Range and Doppler Map (RDM) is shown in Figure 3.4.

Compare Figure 3.4 and Figure 3.3, we observe that the code diversity frame is effective in reducing the Doppler-induced ridge power. Even the peak decrease about 3dB (the result of sacrificing one period for accumulation), the benefit of such a frame scheme is still significant. Besides, we notice that spreading effect results in a little bit floor rise and reduced peak power. The slightly reduced sharpness of the peak along the velocity axis is negligible and does not significantly impact overall performance.

3.3.4 Comparison between State-of-the-Art Frame Design and Code Diversity Frame Design

In this section, we compare the two frame designs thoroughly. The simulation setup and target characteristics remain the same as those outlined in Table 3.1. We firstly delve into code diversity frame's ability to attenuate sidelobes, and then conclude its limitations.

- **Ability to Attenuate Sidelobe**

To clearly observe the effect of sidelobe attenuation, we plot the range cut in the desired velocity bin and in other velocity bins for both the state-of-the-art and code diversity frames in Figure 3.5 and Figure 3.6 respectively. From the range cut in the desired velocity bin, we observe that the peak power decrease about 3dB which is as expected due to the sacrifice in accumulation number. Besides, the code diversity frame structure significantly reduces the Doppler-induced ridge power from 18.56 dB to -1.02 dB, achieving approximately 19 dB attenuation. However, when examining other

velocity bins, we observe a rise in the floor level (from -4.09dB to -0.73dB), as shown in Figure 3.6. This is expected, as power does not disappear but is instead spread out, resulting in the observed floor rise.

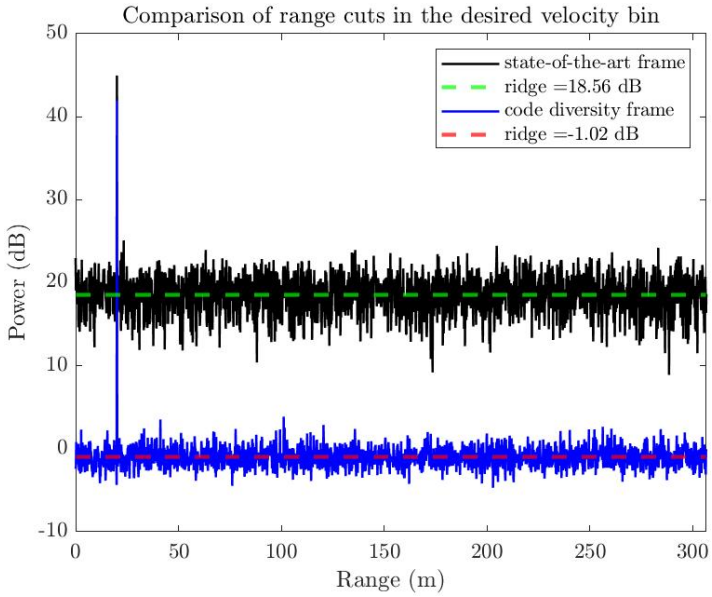

Figure 3.5: Range cut in the desired velocity bin

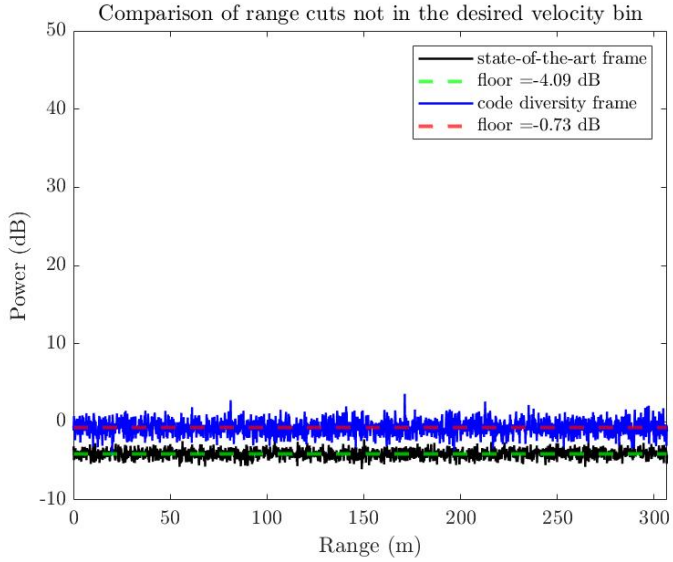

Figure 3.6: Range cut not in the desired velocity bin

To investigate the sidelobe attenuation ability and verify the principle behind floor rise, we conducted several experiments under various target RCS conditions and slow-time sizes. The simulation results for a slow-time size of $M = 198$ are plotted below. From the results, we find that the maximum ridge attenuation is 23.16 dB, close to

the expected $10log_{10}198 = 22.96$ dB. Besides, the floor rise increases with an increase of the RCS of the target. After it reaches the maximum ridge attenuation, the floor rises linearly with the target RCS. To further validate the conclusion, we did another experiment for $M = 64$, and the result is shown in Figure 3.8. From it, we again see the same floor rise pattern, and the maximum ridge attenuation here is 17.81 dB, close to the expected $10log_{10}64 = 18.06$ dB.

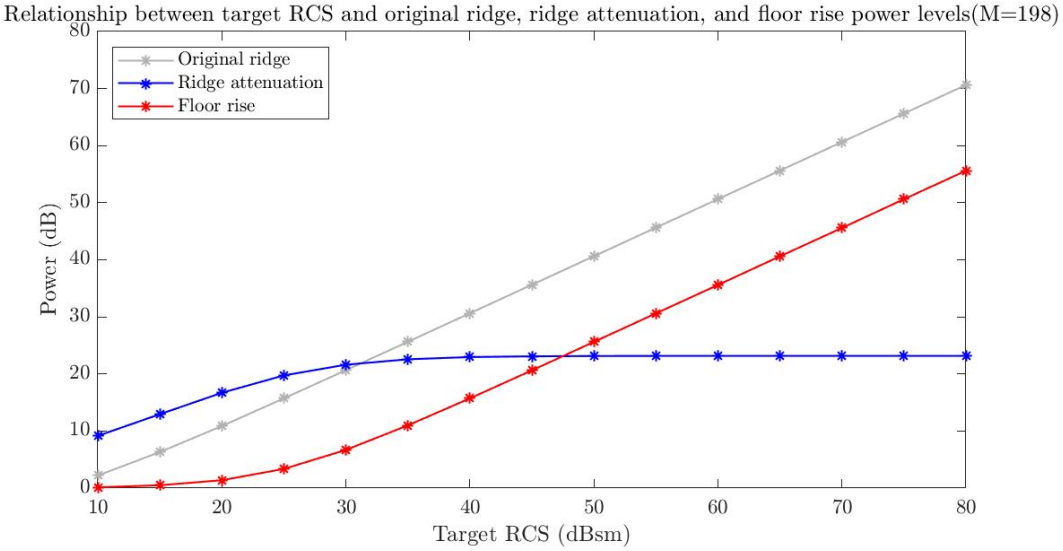

Figure 3.7: Simulation results for $M = 198$

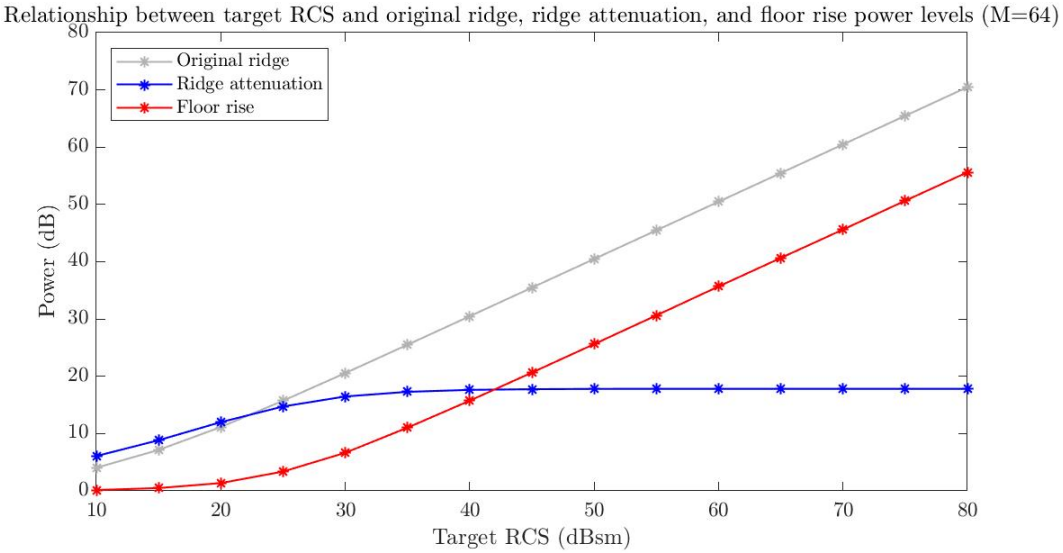

Figure 3.8: Simulation results for $M = 64$

In conclusion, it is evident that the code diversity frame design effectively reduces the Doppler-induced ridge power, resulting in significant sidelobe attenuation. The maximum sidelobe attenuation is related to the slow time size M. However, this comes

at the cost of a rising floor in other velocity bins, which aligns with the principle that the power distribution leads to an overall increase in the noise floor.

- **Limitations of Code Diversity Frame Design**

Even though the code diversity frame design demonstrates significant capability in attenuating sidelobes, it has three main limitations:

1. As mentioned before, the code diversity frame design can cause a rising floor in other velocity bins. This trade-off between ridge attenuation and floor rise must be carefully considered to ensure optimal radar system performance in target detection and Doppler processing.

2. The sequence set size for the state-of-the-art frame design is limited to N_{tx}, but it increases to $N_{tx}M$for the code diversity frame design. Given that the slow time size M is usually very large to achieve higher velocity resolution, and sequences must have good cross- and auto-correlation characteristics, such a large sequence set size is challenging to satisfy with current sequences. This limitation results in the frame being unsuitable for larger MIMO systems, which is the most significant drawback.

In the next section, we will explore improved frame designs aimed at overcoming the sequence set size limitation. We will also apply the enhanced code diversity frame design to MIMO systems to evaluate its effects and potential benefits.

3.4 Frame Design for Large MIMO Systems

From the previous analysis, the effectiveness of the code diversity method in attenuating sidelobes lies in transmitting different sequences along slow time. To maintain this characteristic, each transmitter needs to transmit M different sequences along slow time. However, the structure for several transmitters remains undetermined.

Therefore, we propose two novel frame designs to effectively apply the code diversity frame design to MIMO systems. These designs significantly reduce the sequence set size requirement from $N_{tx}M$ to M, making it feasible to utilize Gold sequences. These improvements address the limitations of previous designs, enabling more efficient and scalable implementations in large MIMO systems.

3.4.1 Proposed Frame Design 1

The proposed frame design 1 introduces a significant improvement over the original code diversity method by utilizing a cyclic shift approach. In this design, each transmitter (TX) in the system employs a unique set of code sequences. Subsequent transmitters do not alter the code sequences themselves but instead cyclically shift the order in which these sequences are used. For example, if TX 1 uses the sequence $s_1, s_2, \ldots, s_{M-1}, s_M$, then TX 2 will use the sequence $s_2, s_3, \ldots, s_M, s_1$, and so forth. This approach reduces the required sequence set size from $N_{tx}M$ to M. The frame design is illustrated in Figure 3.9.

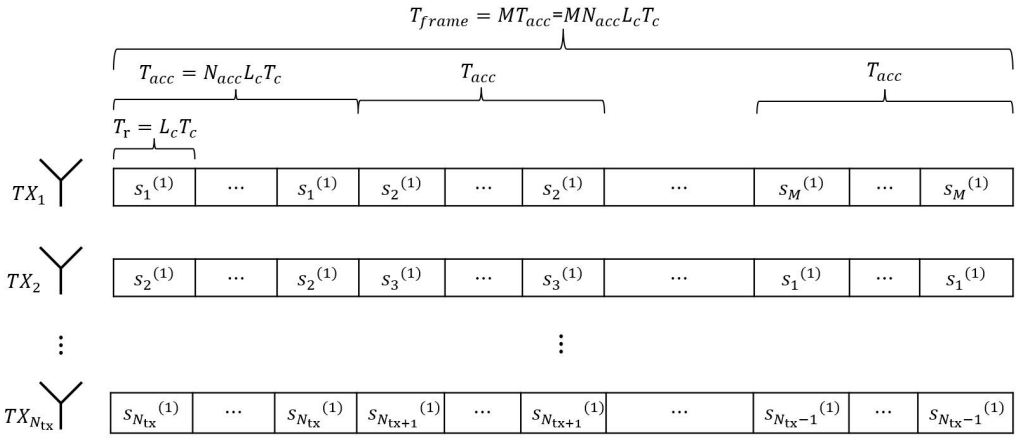

Figure 3.9: Proposed frame design 1

We maintain the assumption of a single target, represented by (R_0, v_0, θ_0). Based on the cyclically shifted frame scheme, we have $c_n^{(i,m)} = c_n^{(1,m+i-1)}$.

- **Range Processing**

Here, we still specifically consider the correlation with the code transmitted by the i_{th} transmitter, and we obtain the correlation result

$$\begin{aligned} r_{i,j}[\tau, m] &= \tilde{\beta}_0 \phi_{R,\theta_0}^{j-1} \sum_{n_{acc}=1}^{N_{acc}-1} e^{j2\pi f_{d,0} n_{acc} T_r} \sum_{i=1}^{N_{tx}} \phi_{T,\theta_0}^{i-1} \sum_{n=0}^{L_c-1} c_{n-\hat{\tau}_0}^{(1,m+i-1)} e^{j2\pi f_{d,0} n T_c} c_{n-\tau}^{(1,m+i-1)} \\ &= \tilde{\beta}_0 \phi_{R,\theta_0}^{j-1} \sum_{n_{acc}=1}^{N_{acc}-1} e^{j2\pi f_{d,0} n_{acc} T_r} \sum_{i=1}^{N_{tx}} \phi_{T,\theta_0}^{i-1} \tilde{r'}_{1,m}[\tau] \end{aligned} \tag{3.14}$$

where $\tilde{r'}_{1,m}[\tau] = \sum_{n=0}^{L_c-1} c_{n-\hat{\tau}_0}^{(1,m+i-1)} e^{j2\pi f_{d,0} n T_c} c_{n-\tau}^{(1,m+i-1)}$.

- **Velocity Processing**

Focus on the desired range bin $\hat{\tau}$, and keep the assumption $k = \hat{k_d} + \Delta_k$, the DFT result is given by:

$$
\begin{aligned}
\mathcal{R}_{i,j}[\hat{\tau},\Delta_k] &= \tilde{\beta}_0\phi_{R,\theta_0}^{j-1}\sum_{n_{acc}=1}^{N_{acc}-1} e^{j2\pi f_{d,0}n_{acc}T_r}\sum_{m=0}^{M-1}\sum_{i=1}^{N_{tx}}\phi_{T,\theta_0}^{i-1}\tilde{r'}_{1,m}[\hat{\tau}]e^{-j\frac{2\pi}{M}m\Delta_k} \\
&= \tilde{\beta}_0\phi_{R,\theta_0}^{j-1}\sum_{n_{acc}=1}^{N_{acc}-1} e^{j2\pi f_{d,0}n_{acc}T_r}\sum_{m=0}^{M-1}\sum_{i=1}^{N_{tx}}\phi_{T,\theta_0}^{i-1}\tilde{r'}_{1,m}[\hat{\tau}]e^{-j\frac{2\pi}{M}(m+i-1)\Delta_k}e^{j\frac{2\pi}{M}(i-1)\Delta_k} \\
&= \tilde{\beta}_0\phi_{R,\theta_0}^{j-1}\sum_{n_{acc}=1}^{N_{acc}-1} e^{j2\pi f_{d,0}n_{acc}T_r}\sum_{m=0}^{M-1}\sum_{i=1}^{N_{tx}}\phi_{T,\theta_0}^{i-1}\tilde{r}_{1,m}[\hat{\tau}]e^{-j\frac{2\pi}{M}m\Delta_k}e^{j\frac{2\pi}{M}(i-1)\Delta_k} \\
&= \tilde{\beta}_0\phi_{R,\theta_0}^{j-1}\sum_{n_{acc}=1}^{N_{acc}-1} e^{j2\pi f_{d,0}n_{acc}T_r}\sum_{i=1}^{N_{tx}}\phi_{T,\theta_0}^{i-1}e^{j\frac{2\pi}{M}(i-1)\Delta_k}\left(\sum_{m=0}^{M-1}\tilde{r}_{1,m}[\hat{\tau}]e^{-j\frac{2\pi}{M}m\Delta_k}\right)
\end{aligned}
\tag{3.15}
$$

- **Analysis**

Note that $\tilde{r}_{i,m}[\tau]$ which is dependent on m has been kept. As mentioned before, the Doppler-induced phase shift affects each sequence differently, summing the pulses together prevents these phase shift effect from aligning constructively, thereby reducing the sidelobe level.

Compared $\mathcal{R}_{1,j}[\hat{\tau},\Delta_k]$ to that given in Eq.(3.13), the difference lies in replacing $\sum_{i=1}^{N_{tx}}\phi_{T,\theta_0}^{i-1}$ with $\sum_{i=1}^{N_{tx}}\phi_{T,\theta_0}^{i-1}e^{j\frac{2\pi}{M}(i-1)\Delta_k}$. This replacement results in summing the original frequency response from the first transmitter and the phase-shifted versions of these responses from subsequent transmitters. This phase-shifting introduces additional sidelobe peaks due to the constructive interference of the shifted frequency responses, as illustrated in Figure 3.10. These extra sidelobe peaks degrade the performance of sidelobe attenuation, which is the primary advantage of the code diversity method.

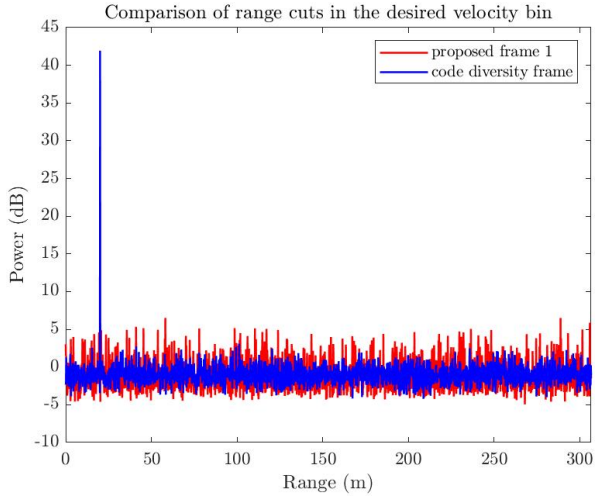

Figure 3.10: Range cut comparison: proposed frame design 1 vs. code diversity frame

3.4.2 Proposed Frame Design 2

The proposed frame design 2 utilizes a Hadamard matrix of order N_{tx}. Each transmitter's sequence is assigned based on a row of the Hadamard matrix, ensuring orthogonality and maintaining the code diversity over slow time. To illustrate this more clearly, based on the Hadamard matrix of order 4, Figure 3.11 illustrates the frame scheme for $N_{tx} = 4$ and $N_{acc} = 2$, .

$$H_4 = \begin{pmatrix} 1 & 1 & 1 & 1 \\ 1 & -1 & 1 & -1 \\ 1 & 1 & -1 & -1 \\ 1 & -1 & -1 & 1 \end{pmatrix}$$

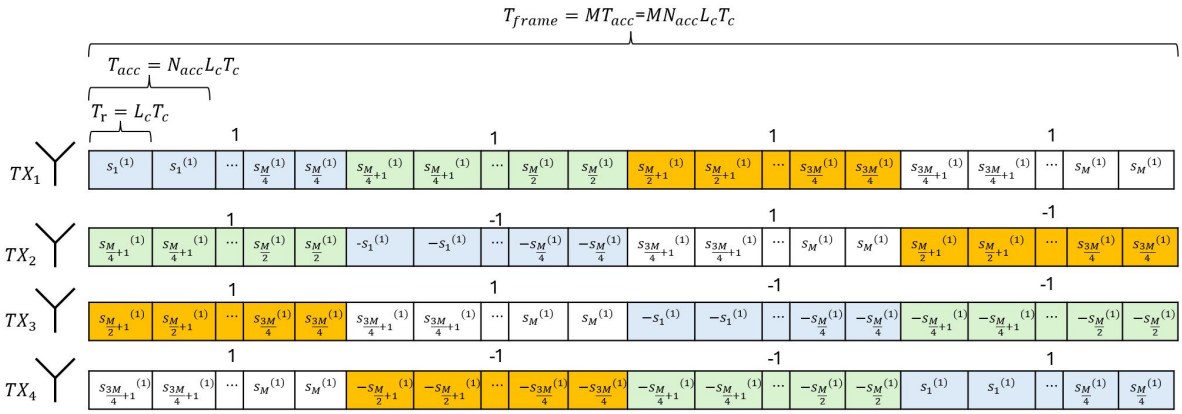

Figure 3.11: Proposed frame design 2

- **Range Processing**

To make the analysis more clear, we use frame scheme for $N_{tx} = 2$ and $N_{acc} = 2$, which is shown in Figure 3.12.

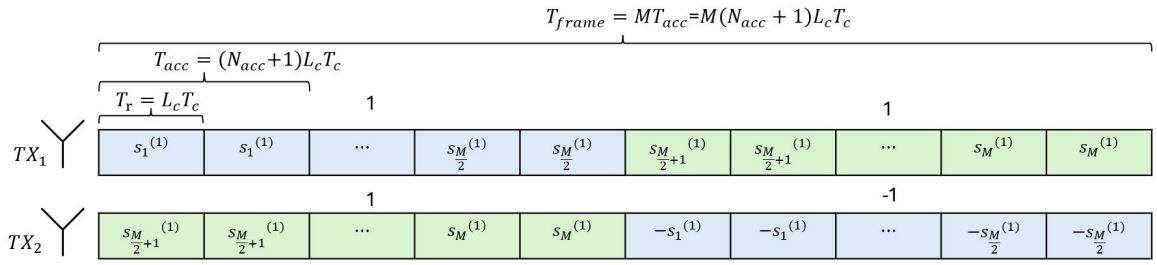

Figure 3.12: Proposed frame design 2 for $N_{tx} = 2$

The correlation result is given as:

$$\begin{aligned} r_{i,j}[\tau, m] &= \tilde{\beta}_0 \phi_{R,\theta_0}^{j-1} e^{j2\pi f_{d,0}(m+1)T_r} \sum_{i=1}^{N_{tx}} \phi_{T,\theta_0}^{i-1} \sum_{n=0}^{L_c-1} c_{n-\hat{\tau_0}}^{(i,m)} e^{j2\pi f_{d,0} n T_c} c_{n-\tau}^{(i,m)} \\ &= \tilde{\beta}_0 \phi_{R,\theta_0}^{j-1} e^{j2\pi f_{d,0}(m+1)T_r} \sum_{i=1}^{N_{tx}} \phi_{T,\theta_0}^{i-1} \tilde{r}_{i,m}[\tau] \end{aligned} \tag{3.16}$$

where $\tilde{r}_{i,m}[\tau] = \sum_{n=0}^{L_c-1} c_{n-\hat{\tau_0}}^{(i,m)} e^{j2\pi f_{d,0} n T_c} c_{n-\tau}^{(i,m)}$, and $c_n^{(i,m)}$ follows

$$c_n^{(i,m)} = \begin{cases} c_n^{(1,m)} & \text{for } i = 1, \\ c_n^{(1,m+\frac{M}{2})} & \text{for } i = 2 \text{ and } m < \frac{M}{2}, \\ -c_n^{(1,m-\frac{M}{2})} & \text{for } i = 2 \text{ and } m \geq \frac{M}{2}. \end{cases}$$

- **Velocity Processing**

Based on the same assumption mentioned before, we still focus on the desired range bin $\hat{\tau}$ and take $k = \hat{k_d} + \Delta_k$ where cell $\hat{k_d}$ satisfies $\hat{k_d} = M f_{d,0} T_r$. The DFT result is then given by:

$$\begin{aligned} \mathcal{R}_{i,j}[\hat{\tau}, \Delta_k] &= \tilde{\beta}_0 \phi_{R,\theta_0}^{j-1} e^{j2\pi f_{d,0} T_r} \left[\sum_{m=0}^{M-1} \tilde{r}_{1,m}[\hat{\tau}] e^{-j\frac{2\pi}{M} m \Delta_k} + \sum_{m=0}^{M-1} \phi_{T,\theta_0} \tilde{r}_{2,m}[\hat{\tau}] e^{-j\frac{2\pi}{M} m \Delta_k} \right] \\ &= \tilde{\beta}_0 \phi_{R,\theta_0}^{j-1} e^{j2\pi f_{d,0} T_r} \left[\sum_{m=0}^{M-1} \sum_{n=0}^{L_c-1} c_{n-\hat{\tau}_0}^{(1,m)} e^{-j2\pi f_{d,0} n T_c} c_{n-\hat{\tau}}^{(1,m)} e^{-j\frac{2\pi}{M} m \Delta_k} \right. \\ &\quad + \phi_{T,\theta_0} \sum_{m=0}^{\frac{M}{2}-1} \sum_{n=0}^{L_c-1} c_{n-\hat{\tau}_0}^{(1,m+\frac{M}{2})} e^{-j2\pi f_{d,0} n T_c} c_{n-\hat{\tau}}^{(1,m+\frac{M}{2})} e^{-j\frac{2\pi}{M}(m+\frac{M}{2})\Delta_k} e^{j\pi\Delta_k} \\ &\quad \left. + \phi_{T,\theta_0} \sum_{m=\frac{M}{2}}^{M-1} \sum_{n=0}^{L_c-1} c_{n-\hat{\tau}_0}^{(1,m-\frac{M}{2})} e^{-j2\pi f_{d,0} n T_c} c_{n-\hat{\tau}}^{(1,m-\frac{M}{2})} e^{-j\frac{2\pi}{M}(m-\frac{M}{2})\Delta_k} e^{-j\pi\Delta_k} \right] \\ &= \tilde{\beta}_0 \phi_{R,\theta_0}^{j-1} e^{j2\pi f_{d,0} T_r} \left[\sum_{m=0}^{M-1} \tilde{r}_{1,m}[\hat{\tau}] e^{-j\frac{2\pi}{M} m \Delta_k} + \phi_{T,\theta_0} e^{j\pi\Delta_k} \sum_{m=\frac{M}{2}}^{M-1} \tilde{r}_{1,m}[\hat{\tau}] e^{-j\frac{2\pi}{M} m \Delta_k} \right. \\ &\quad \left. + \phi_{T,\theta_0} e^{-j\pi\Delta_k} \sum_{m=0}^{\frac{M}{2}-1} \tilde{r}_{1,m}[\hat{\tau}] e^{-j\frac{2\pi}{M} m \Delta_k} \right] \end{aligned} \tag{3.17}$$

- **Analysis**

Note that $\tilde{r}_{i,m}[\tau]$ which is dependent on m has been kept. and summing the pulses together prevents these phase shift effect from aligning constructively, thereby reducing the sidelobe level.

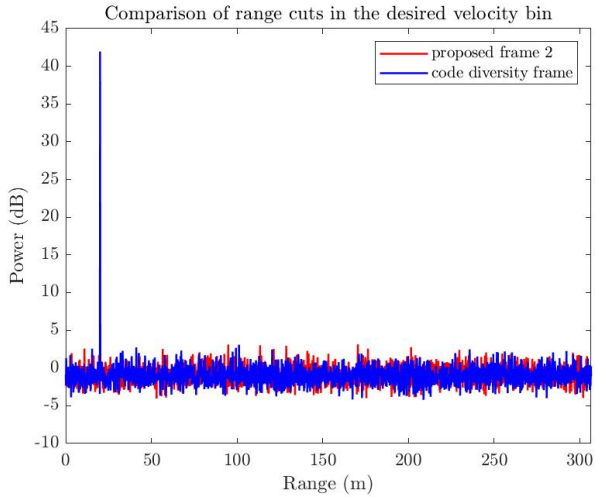

Figure 3.13: Range cut comparison: proposed frame design 2 vs. code diversity frame

The difference from the proposed frame 1 lies in the fact that the two components $\phi_{T,\theta_0} e^{-j\pi\Delta_k} \sum_{m=0}^{\frac{M}{2}-1} \tilde{r}_{1,m}[\hat{\tau}] e^{-j\frac{2\pi}{M}m\Delta_k}$ and $\phi T, \theta_0 e^{j\pi\Delta_k} \sum_{m=0}^{\frac{M}{2}-1} \tilde{r}_{1,m}[\hat{\tau}] e^{-j\frac{2\pi}{M}m\Delta_k}$ cannot be combined into a single summation from $m = 0$ to $m = M - 1$, except for $\Delta_k = 0$. This prevents the summing of phase-shifted versions from subsequent transmitters and, as a result, avoids the increased sidelobes observed in the proposed frame design 1, as shown in Figure 3.13

Therefore, the proposed frame design 2 not only reduces the sequence set size requirement from $N_{tx}M$ to M but also avoids introducing extra sidelobes, thus maintaining the performance of sidelobe attenuation.

3.5 Simulation Scenarios: Compare code Diversity Frame and two Proposed Frames

Range sidelobe attenuation is crucial for detecting weak targets, such as pedestrians hidden behind strong targets like trucks. To evaluate the effectiveness of the two proposed methods and compare their performances, we explore several scenarios. The target characteristics used for simulation are outlined in Table 3.2.

Table 3.2: Target Characteristics

Target 1		**Target 2**	
Radar Cross Section	-5 dBsm	Radar Cross Section	40 dBsm
Distance: R_1	10 m	Distance: R_2	15 m
Relative velocity: v_1	5 m/s	Relative Relative: v_2	5 m/s
Angular: θ_1	0°	Angular: θ_2	0°

3.5.1 Simulation 1: small slow time size M

The simulation setup is stated in Table 3.3, and the range cut comparison of the four frame schemes in desired range cut for Scenario 1 is shown in Figure 3.14.

Table 3.3: Simulation Setup and Target Characteristics

Simulation Setup	
MIMO: $N_{tx} \times N_{rx}$	8×8
Slow time size: M	198
Accumulation number: N_{acc}	2
'Gold' code length: L_c	2047

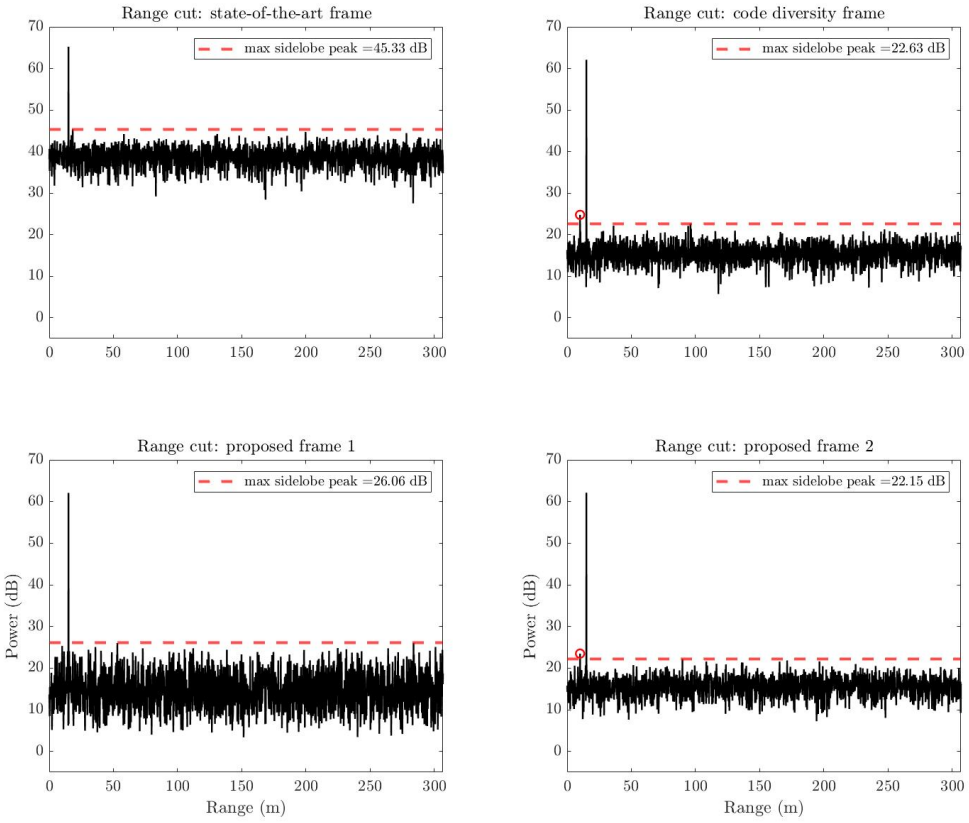

Figure 3.14: Range cut comparison of the 4 frame schemes

From this figure, we observe that the code diversity frame and the two proposed frames, based on the code diversity principle, are effective in attenuating sidelobe levels. Compared to the state-of-the-art frame, they achieve about 22 dB sidelobe attenuation even it scarifies about 3dB peak power for $N_{acc} = 2$ case. Such a sacrifice will decrease with the increase of N_{acc}. It is self-evident that the worst case with smallest N_{acc}, the attenuation in range sidelobe level is still significant which exemplifies the effectiveness

of code diversity principle. Additionally, while both proposed frames help reduce the set size requirement, proposed frame 2 performs better in sidelobe attenuation. Specifically, proposed frame 2 suppresses the sidelobe peak by about 4 dB more than proposed frame 1, providing a higher dynamic range. This enhancement enables the detection of weak targets behind strong targets. In conclusion, only the code diversity frame and proposed frame 2 are successful in detecting the weak target positioned behind the truck.

3.5.2 Simulation 2: large slow time size M

Here, we utilize the same target characteristics as listed in Table 2.3, but we increase the slow time size M, which is not feasible for the code diversity frame. Thus, we only compare the performance of the two proposed frames. The simulation setup is outlined in Table 3.4, and the range cut comparison of the two proposed frames is shown in Figure 3.15.

Table 3.4: Simulation Setup and Target Characteristics

Simulation Setup	
MIMO: $N_{tx} \times N_{rx}$	8×8
Slow time size: M	1022
Accumulation number: N_{acc}	2
'Gold' code length: L_c	2047

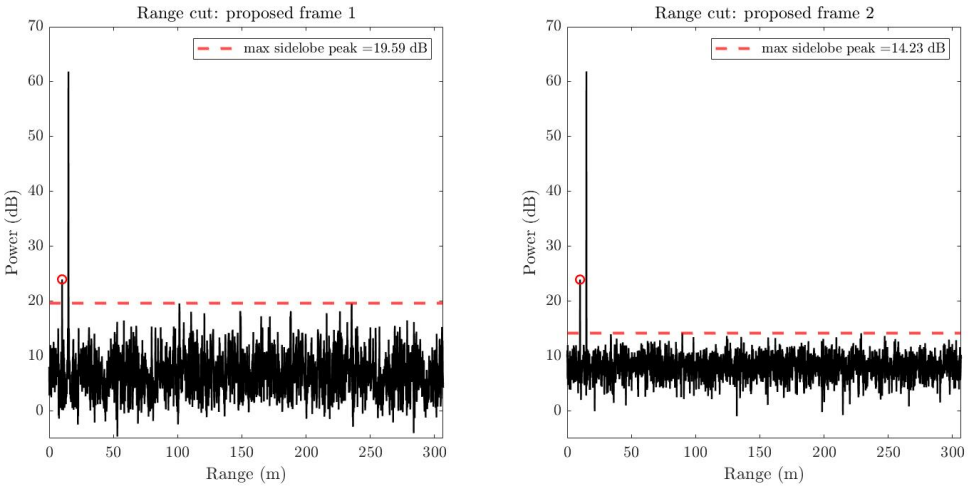

Figure 3.15: Range cut comparison: proposed frame design 1 vs. proposed frame design 2

From this figure, we observe that both frame designs are effective in detecting the weak target. However, when comparing maximum sidelobe peaks, we find that proposed frame 2 performs better, indicating a 5 dB lower sidelobe peak power. This suggests that proposed frame 2 could be more effective in challenging circumstances.

To validate the effectiveness of the two frame designs in tougher conditions, we decrease the radar cross section of target 1 from -5 dBsm to -10 dBsm, making it harder

to detect. The simulation result is shown in Figure 3.16, and we find that the weaker target is hidden in the sidelobe for proposed frame 1. However, with proposed frame 2, it is still possible to detect the weaker target. This enhancement makes proposed frame 2 more suitable for detecting weak targets behind strong targets.

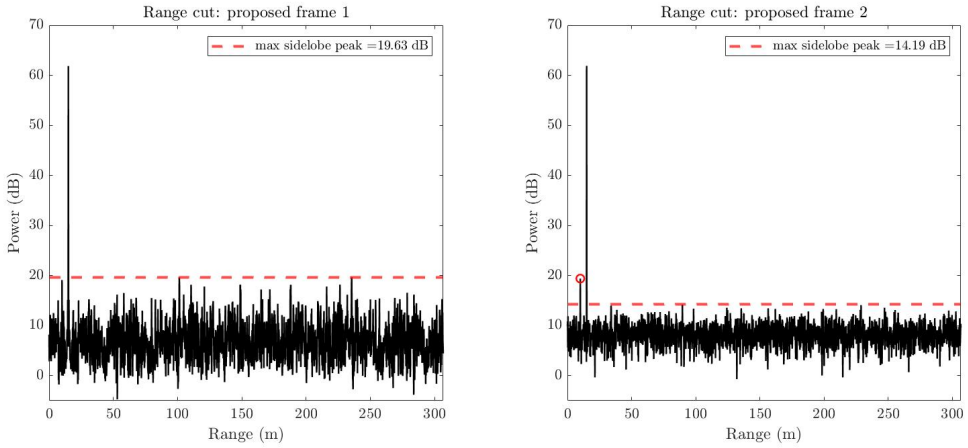

Figure 3.16: Range cut comparison (tougher conditions): proposed frame design 1 vs. proposed frame design 2

3.5.3 Simulation 3: code sequence family change to 'APAS'

Here, we aim to determine if the proposed frame is applicable to other code families. We utilize the same target characteristics as outlined in Table 3.2, but change the code family to 'APAS'. To maintain the effective range, we select a code length of $L_c = 4080$, which corresponds to an effective length of $L_c^{eff} = 2039$. The set size of the APAS sequence with $L_c = 4080$ is 256, supporting M to still be 198. Therefore, the simulation setup is shown in Table 3.5. The comparison of the two proposed frame structures in range cut is shown in Figure 3.17.

Table 3.5: Simulation Setup and Target Characteristics

Simulation Setup	
MIMO: $N_{tx} \times N_{rx}$	8×8
Slow time size: M	198
Accumulation number: N_{acc}	2
'APAS' code length: L_c	4080

From the figure, we find that the two proposed frame designs are still applicable for APAS sequences. The comparison between the two frame schemes demonstrates that proposed frame 2 continues to perform better in terms of sidelobe attenuation and weak target detection. Specifically, proposed frame 2 shows lower sidelobe levels, which facilitates the detection of weaker targets that are obscured by stronger targets in the case of proposed frame 1.

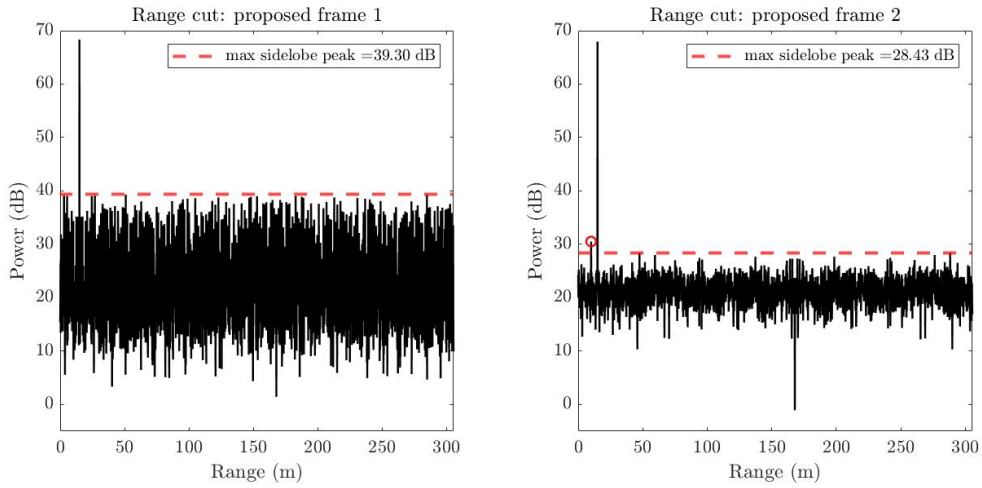

Figure 3.17: Range cut comparison (APAS): proposed frame design 1 vs. proposed frame design 2

3.6 Conclusion

In this chapter, we explored advanced frame designs to mitigate Doppler-induced range sidelobes in PMCW radar systems. We examined the state-of-the-art frame, which transmits the same sequence for all slow times, analyzing the range and velocity processing to understand the cause of increased sidelobe levels in the range profile. We then investigated the code diversity frame, which transmits different sequences for different slow times and transmitters. Our analysis highlighted its advantage in preventing the constructive alignment of phase shifts, thereby reducing sidelobe levels. However, this approach has several limitations: increased floor power, slightly reduced velocity resolution, and the main limitation—the sequence set size increases to $N_{tx}M$. Given that the slow time size M is usually very large to achieve higher velocity resolution, and sequences must have good cross- and auto-correlation characteristics, such a large sequence set size is challenging to satisfy with current sequences. This limitation makes the frame unsuitable for larger MIMO systems, which is the most significant drawback.

To address this, we proposed two novel frame designs to effectively apply the code diversity frame design to MIMO systems, reducing the sequence set size requirement from $N_{tx}M$ to M.

- **Proposed Frame Design 1:** This design utilizes a cyclic shift approach. Each transmitter (TX) in the system employs a unique set of code sequences, with subsequent transmitters cyclically shifting the order of these sequences. However, our analysis revealed that this scheme introduces extra sidelobe peaks, which degrade the frame's advantage in sidelobe attenuation.

- **Proposed Frame Design 2:** Based on the Hadamard matrix, this design assigns each transmitter's sequence based on a row of the Hadamard matrix, ensuring orthogonality and maintaining code diversity over slow time. Our analysis concluded that this frame does not introduce extra sidelobe peaks like frame 1. Simulations,

including scenarios with weak targets behind strong targets, validated that frame 2 outperforms frame 1 in sidelobe attenuation, offering an enhanced dynamic range to detect weak targets and making it more suitable for large MIMO radar systems.

These findings have significant implications for PMCW radar systems, enabling better target detection and Doppler shift mitigation with reduced computational complexity. The proposed frame design 2 offers a scalable solution for large MIMO systems, facilitating their application in advanced automotive radar technologies. This research paves the way for further advancements in radar signal processing, enhancing both performance and reliability in practical applications.

4 Conclusions and Future Work

4.1 Conclusions

The development of Advanced Driver Assistance Systems (ADAS) has significantly advanced automotive safety and performance. ADAS applications require increasingly sophisticated radar systems capable of high detection accuracy, resolution, and processing speed. Traditional analog radar systems face limitations in meeting these stringent requirements, driving the transition to digital radar systems. In this context, Phase Modulated Continuous Wave (PMCW) radar has emerged as a promising technology.

PMCW radar systems offer several advantages, such as no range and Doppler coupling, high range resolution, robustness against interference, and simplified hardware design. However, they also face significant challenges, including Doppler-induced range sidelobes and computational complexity. This thesis focuses on addressing these challenges to enhance the performance of PMCW radar systems.

- **Adaptive Block FFT Correlation Method:** The traditional FFT based correlator with complexity $\mathcal{O}(L_c log_2 L_c)$ can hinder radar performance due to increased processing time and resource consumption. We introduced the adaptive block FFT correlation method to address the high computational complexity of traditional FFT-based correlators. By dynamically determining processing blocks based on initial range computations and other real-time inputs, this method significantly reduces computational load. Simulation results demonstrated that the adaptive block FFT method improves processing efficiency, reducing memory and maintaining high detection accuracy. It ensures efficient real-time data processing, crucial for autonomous driving and advanced driver assistance features.

- **Enhanced Frame Design to Reduce Range Sidelobes:** Doppler effects degrade the orthogonality of binary codes, leading to decreased target peak power and increased range sidelobes. Traditional approaches to mitigate Doppler effects involve compensating for frequency shifts, which increases computational complexity. Then the code diversity method is introduced as a low-complexity alternative. Through comprehensive analysis and simulations, we showed that the code diversity frame design effectively attenuates range sidelobes, improving the peak-to-sidelobe ratio. However, it requires a huge suitable sequence set size which is hard to achieve for MIMO system. Therefore, we proposed novel frame designs for MIMO systems, which leverage cyclic shifts and Hadamard matrices. They were shown to significantly reduce the sequence set size requirement while maintaining sidelobe attenuation performance. After comparison, the proposed method based on Hadamard matrices performs better. It improves the radar's ability to accurately detect both large and small targets, essential for applications

like pedestrian detection behind strong reflectors, thereby significantly improving safety. Reducing the sequence set size requirement makes these methods scalable for large MIMO radar systems, supporting the complex demands of ADAS.

4.2 Future Work

Future research could explore several avenues to further enhance PMCW radar systems for ADAS:

- **Investigating Alternative Frame Designs:** We could explore additional frame designs that might achieve similar or improved effects compared to the proposed methods. Investigating new approaches for sidelobe attenuation could offer alternative strategies that might be more efficient or effective in other scenarios where spillover is present. This exploration should include both theoretical analysis and practical simulations to validate potential benefits.
- **Incorporating Quiet Periods in Frame Design:** Quiet periods could be introduced within the frame design. These periods would allow sensors to detect and measure potential mutual interference, thereby mitigating its impact. By sensing and adapting to interference, the radar system can dynamically adjust its operation to enhance overall performance and reliability, especially in environments with multiple radar sources.
- **Windowing Techniques:** The proposed correlation methods could be combined with windowing techniques. Windowing can further attenuate sidelobes and improve the signal-to-noise ratio (SNR). Implementing various windowing functions and evaluating their impact on sidelobe reduction and radar performance will provide deeper insights into optimizing PMCW radar systems.
- **Extensive Real-World Simulations:** We could extend the simulation scenarios from point targets to point clouds. This enhancement will provide more comprehensive and realistic simulations, better reflecting actual radar performance and challenges in real-world scenarios. Simulating complex environments with multiple scatterers will help in understanding the interactions and performance of the radar system in dynamic and cluttered environments.

By exploring these future research directions, we can further advance PMCW radar technology, enhancing its effectiveness and reliability in supporting the sophisticated requirements of ADAS. These efforts will contribute to the development of safer and more efficient autonomous driving systems.

Bibliography

[1] M. E. Warren, "Automotive lidar technology," in *2019 Symposium on VLSI Circuits*, pp. C254–C255, 2019.

[2] A. Bourdoux, K. Parashar, and M. Bauduin, "Phenomenology of mutual interference of fmcw and pmcw automotive radars," in *2017 IEEE Radar Conference (RadarConf)*, pp. 1709–1714, 2017.

[3] "Sae standard j3016: Taxonomy and definitions for terms related to driving automation systems for on-road motor vehicles," 2021.

[4] M. Galvani, "History and future of driver assistance," *IEEE Instrumentation & Measurement Magazine*, vol. 22, no. 1, pp. 11–16, 2019.

[5] F. Roos, J. Bechter, C. Knill, B. Schweizer, and C. Waldschmidt, "Radar sensors for autonomous driving: Modulation schemes and interference mitigation," *IEEE Microwave Magazine*, vol. 20, no. 9, pp. 58–72, 2019.

[6] J. Li and P. Stoica, "Mimo radar with colocated antennas," *IEEE Signal Processing Magazine*, vol. 24, no. 5, pp. 106–114, 2007.

[7] B. Harker, Z. Dobrosavljevic, E. Craney, C. Tubb, and G. Harris, "Dynamic range improvements and measurements in radar systems," *IET Radar, Sonar & Navigation*, vol. 1, no. 6, pp. 398–406, 2007.

[8] A. Bourdoux, K. Parashar, and M. Bauduin, "Phenomenology of mutual interference of fmcw and pmcw automotive radars," in *2017 IEEE Radar Conference (RadarConf)*, pp. 1709–1714, 2017.

[9] M. Caffa, F. Biletta, and R. Maggiora, "Binary-phase vs. frequency modulated radar measured performances for automotive applications," *Sensors*, vol. 23, no. 11, 2023.

[10] C. Waldschmidt, J. Hasch, and W. Menzel, "Automotive radar — from first efforts to future systems," *IEEE Journal of Microwaves*, vol. 1, no. 1, pp. 135–148, 2021.

[11] U. White, "Digital code modulation (dcm) radar for automotive application," 2020.

[12] J. A. Zhang, F. Liu, C. Masouros, R. W. Heath, Z. Feng, L. Zheng, and A. Petropulu, "An overview of signal processing techniques for joint communication and radar sensing," *IEEE Journal of Selected Topics in Signal Processing*, vol. 15, no. 6, pp. 1295–1315, 2021.

[13] G. Hakobyan and B. Yang, "High-performance automotive radar: A review of signal processing algorithms and modulation schemes," *IEEE Signal Processing Magazine*, vol. 36, no. 5, pp. 32–44, 2019.

[14] A. Khorami, M. B. Dastjerdi, and A. F. Ahmadi, "A low-power high-speed comparator for analog to digital converters," in *2016 IEEE International Symposium on Circuits and Systems (ISCAS)*, pp. 2010–2013, 2016.

[15] A. Bourdoux, U. Ahmad, D. Guermandi, S. Brebels, A. Dewilde, and W. Van Thillo, "Pmcw waveform and mimo technique for a 79 ghz cmos automotive radar," in *2016 IEEE Radar Conference (RadarConf)*, pp. 1–5, 2016.

[16] D. Guermandi, Q. Shi, A. Dewilde, V. Derudder, U. Ahmad, A. Spagnolo, A. Bourdoux, P. Wambacq, and W. van Thillo, "A 79ghz 2×2 mimo pmcw radar soc in 28nm cmos," in *2016 IEEE Asian Solid-State Circuits Conference (A-SSCC)*, pp. 105–108, 2016.

[17] D. Guermandi, Q. Shi, A. Medra, T. Murata, W. Van Thillo, A. Bourdoux, P. Wambacq, and V. Giannini, "19.7 a 79ghz binary phase-modulated continuous-wave radar transceiver with tx-to-rx spillover cancellation in 28nm cmos," in *2015 IEEE International Solid-State Circuits Conference - (ISSCC) Digest of Technical Papers*, pp. 1–3, 2015.

[18] M. Bauduin and A. Bourdoux, "Code diversity for range sidelobe attenuation in pmcw and ofdm radars," in *2021 IEEE Radar Conference (RadarConf21)*, pp. 1–5, 2021.

[19] H. He, J. Li, and P. Stoica, *Waveform design for active sensing systems: a computational approach*. Cambridge University Press, 2012.

[20] L. Welch, "Lower bounds on the maximum cross correlation of signals (corresp.)," *IEEE Transactions on Information Theory*, vol. 20, no. 3, pp. 397–399, 1974.

[21] W. Van Thillo, P. Gioffré, V. Giannini, D. Guermandi, S. Brebels, and A. Bourdoux, "Almost perfect auto-correlation sequences for binary phase-modulated continuous wave radar," in *2013 European Radar Conference*, pp. 491–494, 2013.

[22] A. Turkmani and U. Goni, "Performance evaluation of maximal-length, gold and kasami codes as spreading sequences in cdma systems," in *Proceedings of 2nd IEEE International Conference on Universal Personal Communications*, vol. 2, pp. 970–974 vol.2, 1993.

[23] T. Maeda, S. Kanemoto, and T. Hayashi, "A novel class of binary zero-correlation zone sequence sets," in *TENCON 2010 - 2010 IEEE Region 10 Conference*, pp. 708–711, 2010.

[24] M. Alaee-Kerahroodi, M. Modarres-Hashemi, M. M. Naghsh, B. Shankar, and B. Ottersten, "Binary sequences set with small isl for mimo radar systems," in *2018 26th European Signal Processing Conference (EUSIPCO)*, pp. 2395–2399, 2018.

[25] Y. Chen, R. Lin, and X. Li, "Designing periodic binary sequence sets for mimo pmcw radar systems," in *2023 24th International Radar Symposium (IRS)*, pp. 1–10, 2023.

[26] S. Xu and A. Yarovoy, "Doppler shifts mitigation for pmcw signals," in *2019 International Radar Conference (RADAR)*, pp. 1–5, 2019.

[27] J. Overdevest, F. Jansen, F. Uysal, and A. Yarovoy, "Doppler influence on waveform orthogonality in 79 ghz mimo phase-coded automotive radar," *IEEE Transactions on Vehicular Technology*, vol. 69, no. 1, pp. 16–25, 2020.

[28] K. Lin, Y. E. Wang, C.-K. Pao, and Y.-C. Shih, "A *ka*-band fmcw radar front-end with adaptive leakage cancellation," *IEEE Transactions on Microwave Theory and Techniques*, vol. 54, no. 12, pp. 4041–4048, 2006.

[29] A. Medra, D. Guermandi, K. Vaesen, S. Brebels, A. Bourdoux, W. Van Thillo, P. Wambacq, and V. Giannini, "An 80 ghz low-noise amplifier resilient to the tx spillover in phase-modulated continuous-wave radars," *IEEE Journal of Solid-State Circuits*, vol. 51, no. 5, pp. 1141–1153, 2016.

[30] P. Stagnaro, A. Pandharipande, J. Overdevest, and H. Joudeh, "Mimo digital radar processing with spatial nulling for self-interference mitigation," in *2023 IEEE SENSORS*, pp. 1–4, IEEE, 2023.

[31] M. Bauduin and A. Bourdoux, "Mixed-signal transmitter leakage cancellation for pmcw mimo radar," in *2018 15th European Radar Conference (EuRAD)*, pp. 293–296, 2018.

[32] R. G. Lyons, *Understanding Digital Signal Processing*. Prentice Hall, 3rd ed., 2010.

[33] J. Leclère, C. Botteron, R. Landry, and P.-A. Farine, "Fft splitting for improved fpga-based acquisition of gnss signals," *International Journal of Navigation and Observation*, vol. 2015, pp. 1–12, 2015.